Analyzing Slightly Inclined Cylindrical Binary Fluid Convection via Higher Order Dynamic Mode Decomposition[*]

Arantxa Alonso[†], Isabel Mercader[†], Oriol Batiste[†], and José M. Vega[‡]

Abstract. An extended dynamical system is considered that shows some striking, very complex spatio-temporal patterns. Specifically, we consider superhighway patterns that appear in binary fluid convection in slightly inclined, shallow cylindrical containers. These patterns show a number of parallel thermal lanes, each containing aligned coherent structures that counterpropagate in adjacent lanes. Several types of superhighway convection states have been obtained by direct numerical simulation. The numerical outcomes are analyzed using a recent data processing tool, known as higher order dynamic mode decomposition, which efficiently identifies relevant spatio-temporal patterns in numerically computed data.

Key words. extended dynamical systems, pattern formation, attractors, binary convection, spatio-temporal patterns, data processing tools

MSC codes. 35B36, 35B41, 37N10, 68P05, 80A20

DOI. 10.1137/21M1447416

1. Introduction.

Extended dynamical systems, such as those relevant in *pattern formation*, may lead to very complex spatio-temporal patterns that, frequently, can only be obtained via numerical simulation. Identifying these complex patterns can be very difficult.

Convective flows are of great interest in pattern formation. In binary mixtures, thermal convection promoted by thermal gradients [1] may be enhanced by concentration nonuniformities sustained by the Soret coupling, i.e., by the generation of concentration fluxes due to temperature gradients (Soret effect). The components of miscible ordinary two-component mixtures tend to separate in an imposed thermal gradient, and this separation in turn alters the driving force for convection, giving rise to a variety of convection patterns when driven away from equilibrium by external stresses [2, 3, 4]. Many of the interesting effects in Soret-induced convection originate from the difference in relaxation times between the temperature and the concentration fields, due to the sharp contrast between thermal and solutal diffusivities. The Soret coefficient S_T measures the strength of the Soret coupling, and its sign determines the behavior of the mixture. With $S_T > 0$, the heavier component of the fluid is driven in the direction of lower temperature, while with $S_T < 0$, the heavier component migrates toward the hotter boundary. In this paper, we consider thermal convection in a binary

[†]Departamento de Física, Universitat Politècnica de Catalunya, 08034 Barcelona, Spain (arantxa.alonso@upc.edu, maria.isabel.mercader@upc.edu, oriol.batiste@upc.edu).
[‡]Corresponding author. E.T.S.I. Aeronáutica y del Espacio, Universidad Politécnica de Madrid, 28040 Madrid, Spain (josemanuel.vega@upm.es).

fluid layer heated from below with $S_T > 0$, for which the solutal density variations enhance the thermal density variations and further destabilize the fluid layer heated from below. Since the concentration gradient also contributes to the convective behavior, the onset of convection takes place for smaller heating than in the pure fluid case. The driving mechanisms in binary convection are controlled by two nondimensional numbers: the Rayleigh number Ra, measuring the applied temperature stress, and the separation ratio S, proportional to S_T, which quantifies the solutal driving. Experiments on vertical cylindrical cells performed in the eighties [5, 6] revealed that near onset, the motion is dominated by concentration gradients (*Soret regime*), far from threshold, convection selects structures observed in pure fluid convection (*Rayleigh regime*), and in the cross-over region, complex time-dependent dynamics arises.

In the physical system considered in this work, in addition to the thermodiffusive effects, the convective layer will be slightly tilted and a shear mechanism will be present. The effect of inclination has been widely studied for one-component fluids. Bodenschatz, Pesch, and Ahlers reviewed the main numerical and experimental results obtained during the eighties and nineties in extended layers [7]. The initial focus was on the competition between the longitudinal, transverse, and oblique rolls that arise from the primary bifurcation of the large scale circulatory flow. Later experimental [8, 9] and numerical [10] studies showed that there is a very rich variety of spatio-temporal patterns when the inclination angle is varied. Very recently, Reetz et al. [11, 12] have related the complex time-dependent dynamics observed in inclined convection far beyond onset with the existence of underlying invariant states of the Oberbeck–Boussinesq equations. The authors constructed numerically these invariant states, analyzed their stability, and obtained an extensive bifurcation network connecting them when both heating and inclination are changed.

In this work, we focus on some unexpected patterns encountered in binary convection when a flat container is slightly inclined. Among these, *superhighway convection* (SHC) patterns have been detected, both experimentally [13] and numerically [14], for appropriate values of the involved nondimensional parameters (in particular, the Rayleigh number). SHC patterns arise in the *Soret regime*, where concentration gradients still contribute significantly to the dynamics. Consequently, such flows are not observed in the equivalent single component fluid configuration, even in the case of purely conducting boundaries [15]. In SHC, the temperature field shows objects that are aligned along the inclination direction in parallel (approximately straight) lanes and counter–propagate in adjacent lanes. Thus, these patterns are complex but regular (see the video mentioned in the caption of Figure 4.5). The concentration field, instead, appears to be fairly irregular to the naked eye, which could even see them as showing spatio-temporal chaos (see the video mentioned in the caption of Figure 4.6). This is surprising because the thermal and concentration fields are coupled in the governing equations. In other words, irregularity in the concentration field should be transferred to the thermal field. Understanding this apparent contradiction is one of the objects of the present paper.

Some *periodic superhighway patterns* exhibiting different types of spatio-temporal symmetries have been identified. We call them *symmetric* SHC patterns and they have been found stable only in small regions of the parameter space. More complex patterns, qualitatively similar to symmetric superhighways except that they exhibit amplitude modulation, are more abundant. These patterns will be called *modulated* SHC patterns and seem to be originated via Neimark–Sacker bifurcations [16] and further bifurcations of the symmetric SHC states. In

this paper, we shall consider several representative, numerically obtained patterns for sample values of the Rayleigh number. Each of these will be analyzed using a recent data processing tool known as the *higher order dynamic mode decomposition* (HODMD) [17]. This method decomposes the thermal and concentration fields as Fourier-like expansions that apply to the whole spatial distributions simultaneously. The resulting expansions are to be obtained from a set of spatially discretized *snapshots*, which are instantaneous portraits of the system at equispaced values of time. As such, the method represents an improvement of standard *dynamic mode decomposition* (DMD) [18] (see also [19, 20, 21]). The main difference between standard DMD and HODMD is that the former method assumes that each snapshot depends linearly on the former snapshot, with the linear operator relating both snapshots being constant along the snapshot sequence. The HODMD method, instead, assumes that each snapshot depends linearly, not only on the former snapshot, but also on the last $d-1$ time delayed snapshots, for some index $d > 1$. In this sense, HODMD can be seen as a synergic combination of standard DMD and the advantages [22] that are implicit in Taken's delay embedding theorem [23]. The resulting method is quite robust and gives good results in cases in which standard DMD is not optimal; see [24] for a reader friendly presentation of the method and some of its extensions and multiple applications. Let us mention here that related thermal convection problems, invariant under rotation in rotationally symmetric geometries, have been analyzed [25, 26] using an extension of HODMD, called spatio-temporal Koopman decomposition, developed in [25]. This extension is able to identify rotating traveling and standing waves. However, in the present case, even though the cylindrical container is rotationally symmetric, invariance under rotation is broken by the inclination and plain HODMD is more appropriate.

Using HODMD, the symmetric and modulated superhighways will be analyzed. In particular, for the former patterns, it is found that the spatio-temporally irregular concentration distribution is just the superposition of a spatially irregular temporal mean field and a zero-mean periodic oscillation, which resembles qualitatively the temperature field. Concerning the modulated superhighways, some of them (in narrow ranges of the Rayleigh number) become periodic or quasi-periodic for reasonably large time. However, for most values of the Rayleigh number, modulated orbits turn out to remain very irregular (i.e., neither periodic not quasi-periodic) even for extremely large time. The nature of these three types of modulated super-highways, periodic, quasi-periodic, and irregular, will be uncovered by the HODMD method.

Against this background, the remainder of the paper is organized as follows. The HODMD method will be summarized in section 2, where the relevant formulae to compute the above-mentioned Fourier-like expansions of the temperature and concentration fields will be given. The set of equations governing the binary convection in the slightly inclined circular cylinder will be described in section 3. The abovementioned patterns, namely the symmetric and modulated superhighway oscillations, will be analyzed using HODMD in section 4. The paper ends with some concluding remarks, which will be given in section 5.

2. Higher order dynamic mode decomposition. Although this method applies to the temporal evolution of general, real or complex, vector fields, here for simplicity we consider a real scalar vector field, which in the present context can be either the temperature or the concentration field at the mean slice of the cylindrical container, denoted as q. These fields will depend on two spatial variables (below, the radial and azimuthal coordinates, r and ϕ,

respectively) and also on the time variable t. Dynamic mode decomposition methods (either standard DMD or HODMD) decompose the state variable as

$$(2.1) \qquad q(r, \phi, t) \simeq \sum_{n=1}^{N} a_n u_n(r, \phi) \, \mathrm{e}^{(\delta_n + \mathrm{i}\,\omega_n)\,t},$$

where $a_n \geq 0$ and u_n are the real *mode amplitudes* and the (generally complex) conveniently normalized *spatial modes*, respectively. Here, the modes will be normalized to exhibit unit root mean square (RMS) norm. The real scalars appearing in the exponent, δ_n and ω_n, are the *temporal growth rates* and *frequencies*, respectively. Since the data are real, the various terms in (2.1) must combine in complex conjugate pairs, namely the expansion (2.1) is invariant under the action

$$(2.2) \qquad u_n \to \overline{u}_n \text{ and } \omega_n \to -\omega_n,$$

with the overbar standing hereinafter for the complex conjugate. It must be noted that, as indicated in (2.1), the left- and right-hand sides of this equation are not generally exactly equal to each other (due to mode truncation and other numerical artifacts), but only approximately equal, with the difference between both hopefully very small. When the expansion (2.1) is applied to several scalar variables that are coupled among each other (namely, the temperature and concentration fields in the present context), δ_n and ω_n are typically common (at least very approximately) to these scalar variables. In fact, this will be checked below.

The expansion (2.1) will be obtained in discretized form considering I_1 values of the radial coordinate r, I_2 values of the azimuthal coordinate ϕ, and K values of the temporal coordinate t. Namely, (2.1) is rewritten as

$$(2.3) \qquad T_{i_1 i_2 k} \equiv q(r_{i_1}, \phi_{i_2}, t_k) \simeq \sum_{n=1}^{N} a_n u_n(r_{i_1}, \phi_{i_2}) \, \mathrm{e}^{(\delta_n + \mathrm{i}\,\omega_n)\,t_k},$$

where the K discrete values of time must be equispaced, namely such that

$$(2.4) \qquad t_k = (k-1)\,\Delta t,$$

in terms of the *temporal gap* between consecutive snapshots, $\Delta t > 0$. This is a very important requirement for the methods used below. Note that replacing t_k by t in (2.3) (which involves temporal interpolation) and applying a convenient interpolation in the radial and azimuthal coordinates, the original expansion (2.1) is readily recovered from (2.3).

On the other hand, for transient dynamics converging to an attractor, some of the modes appearing in (2.3) are such that $\delta_n = 0$ (or $|\delta_n|$ very small) and the remaining ones exhibit negative δ_n. Eliminating from the expansion the latter modes permits computing the final attractor (temporal extrapolation [27]). Also, for transient dynamics departing from unstable attractors, some of the growth rates are positive and the method permits identifying the associated instabilities. For attractors, the absolute value of the growth rates is very small. In this case, a good account of how well the expansions (2.1) and (2.3) give the attractor results from a semilogarithmic plot of the amplitudes versus the frequencies, which will be called the

$a - \omega$ *diagram*. This diagram permits identifying the *dominant modes*, namely those modes exhibiting the largest amplitudes, which are relevant to uncover the dynamics.

The *snapshots* appearing in the left-hand side of (2.3) depend on three indexes and, thus, they constitute a third order, $I_1 \times I_2 \times K$ tensor, called the *snapshot tensor*. Constructing the HODMD method for snapshot tensors requires using tensor decomposition methods [28], such as the so-called higher order singular value decomposition, invented by Tucker [29] in 1966 and more recently popularized by de Lathauwer, de Moor, and Vandewalle [30]. This approach is appealing [17] and, moreover, permits constructing a very efficient method to clean noisy artifacts in experimental databases [31].

In this paper, we shall rely on numerical data showing quite small discretization errors. Thus, we shall follow a simpler approach relying on a *snapshot matrix*, which is constructed from the snapshot tensor as follows. The indexes i_1 and i_2 are encompassed into a single index, j. In other words, the snapshot tensor is folded into a *snapshot matrix*, of order $J \times K$, with $J = I_1 I_2$. This permits rewriting (2.3) as

$$(2.5) \qquad A_{jk} \equiv q(r_j, \phi_j, t_k) \simeq \sum_{n=1}^{N} a_n u_n(r_j, \phi_j) \, e^{(\delta_n + i\,\omega_n)\,t_k}.$$

The columns of the snapshot matrix $\mathbf{A}$ (which are vectors of size J) are called the *snapshots* and denoted as $\boldsymbol{v}_k$. Thus, the expansion (2.5) can also be written as

$$(2.6) \qquad \boldsymbol{v}_k \simeq \sum_{n=1}^{N} a_n \boldsymbol{u}_n \, e^{(\delta_n + i\,\omega_n)\,t_k},$$

where the J components of the vectors $\boldsymbol{u}_n$ are $u_n(r_1, \phi_1), \ldots, u_n(r_J, \phi_J)$.

This is the formulation that will be followed below. Once the decomposition (2.5) is obtained, the original tensor decomposition (2.3) is recovered from (2.5) by splitting the index j into the original indexes i_1 and i_2, which results in unfolding the snapshot matrix into the original snapshot tensor. In this case, the expansion (2.5) could in principle be computed using standard DMD [20]. However, this method fails when the *spatial complexity* (defined as the rank of the set of spatial modes) is strictly smaller than the *spectral complexity* (defined as the number of terms that are present in the expansion). In this case, *standard* DMD can be substituted by HODMD, which gives good results for arbitrary values of the spatial and spectral complexities [17].

Standard DMD is a particular case of HODMD for $d = 1$, where the index $d \geq 1$ is defined below. For the present case of relying on a snapshot matrix, the HODMD method proceeds in four steps that are summarized here (see [17] for full details):

1. *First dimension reduction*, which decreases the spatial dimension of the snapshot matrix by taking advantage of the redundancies among the snapshots that are present. This dimension reduction is performed via truncated *singular value decomposition* (SVD) [32], which reduces the spatial dimension from J to $J' < J$. In this way, the $J \times K$ snapshot matrix is approximated as

$$(2.7) \qquad\qquad\qquad \mathbf{A} \simeq \mathbf{A}^{\text{trunc.}} = \boldsymbol{U}\widehat{\mathbf{A}},$$

where the $J \times J'$ matrix $\boldsymbol{U}$ is such that $\boldsymbol{U}^\top \boldsymbol{U} =$ the $J' \times J'$ unit matrix and the $J' \times K$ matrix $\widehat{\mathbf{A}}$ is called the *reduced snapshot matrix*. Note that the SVD singular values have been absorbed in the matrix $\widehat{\mathbf{A}}$. The columns of this matrix, denoted as $\widehat{\boldsymbol{v}}_k$, are vectors of size J', called the *reduced snapshots*. Invoking (2.7) leads to

$$(2.8) \qquad \boldsymbol{v}_k \simeq \boldsymbol{U}\,\widehat{\boldsymbol{v}}_k.$$

The size of the reduced snapshots (which coincides with the number of retained SVD singular values), J', is determined using well-known [32] SVD formulae. In other words, the relative RMS error of the truncated approximation of the snapshot matrix is required to be smaller than some *tunable threshold* ε_1. Thus, we impose that

$$(2.9) \qquad \text{RRMS error} \equiv \frac{\|\mathbf{A} - \mathbf{A}^{\text{trunc.}}\|_{\text{Fro}}}{\|\mathbf{A}\|_{\text{Fro}}} \leq \varepsilon_1,$$

where $\|\cdot\|_{\text{Fro}}$ is the *Frobenius norm* of the matrices, namely the square root of the sum of the squares of the elements of each matrix.

2. *Modified snapshots and second dimension reduction.* We define an index $d \geq 1$, which is a tunable parameter of the method. If $d > 1$, then each reduced snapshot is enlarged considering also the former $d-1$ time-shifted snapshots. The resulting enlarged snapshots, whose size is $d\,J'$, are called the *modified snapshots* and defined as

$$(2.10) \qquad \widetilde{\boldsymbol{v}}_k \equiv \begin{bmatrix} \widehat{\boldsymbol{v}}_k \\ \widehat{\boldsymbol{v}}_{k+1} \\ \dots \\ \widehat{\boldsymbol{v}}_{k+d-2} \\ \widehat{\boldsymbol{v}}_{k+d-1} \end{bmatrix} \quad \text{for } k = 1, \dots, K-d+1.$$

Note that, consistently, $\widetilde{\boldsymbol{v}}_k = \widehat{\boldsymbol{v}}_k$ if $d = 1$. Now, the *modified snapshot matrix* (whose columns are the modified snapshots) is defined as

$$(2.11) \qquad \widetilde{\boldsymbol{V}}_1^{K-d+1} = [\widetilde{\boldsymbol{v}}_1, \widetilde{\boldsymbol{v}}_2, \dots, \widetilde{\boldsymbol{v}}_{K-d+1}].$$

This matrix, whose size is $(d\,J') \times (K-d+1)$, is dimension reduced via truncated SVD, which gives

$$(2.12) \qquad \widetilde{\boldsymbol{V}}_1^{K-d+1} \simeq \widetilde{\boldsymbol{U}}\,\widetilde{\boldsymbol{V}}_1^{*K-d+1},$$

where the $(d\,J') \times \widetilde{N}$ matrix $\widetilde{\boldsymbol{U}}$ is such that $\widetilde{\boldsymbol{U}}^\top \widetilde{\boldsymbol{U}} =$ the $\widetilde{N} \times \widetilde{N}$ unit matrix and the $\widetilde{N} \times (K + d - 1)$ matrix $\widetilde{\boldsymbol{V}}_1^{*K-d+1}$ is called the *reduced-modified snapshot matrix*. The columns of $\widetilde{\boldsymbol{V}}_1^{*K-d+1}$ are called the *reduced-modified snapshots* and denoted as $\widetilde{\boldsymbol{v}}_1^*, \widetilde{\boldsymbol{v}}_2^*, \dots, \widetilde{\boldsymbol{v}}_{K-d+1}^*$. Thus, (2.12) can be rewritten as

$$(2.13) \qquad \widetilde{\boldsymbol{v}}_k \simeq \widetilde{\boldsymbol{U}}\,\widetilde{\boldsymbol{v}}_k^* \text{ for } k = 1, \dots, K-d+1.$$

Note that, as in step 1, the SVD singular values have been absorbed in the reduced-modified snapshots. The number of retained modes (which coincides with the size of the reduced-modified snapshots), $\widetilde{N} \geq J'$, is chosen as we did in step 1, truncating the SVD with the same tunable threshold, ε_1, used there.

3. *Computation of the growth rates and frequencies.* The reduced-modified snapshots computed in the last step are treated via the standard DMD, which relies on the assumption

$$(2.14) \qquad \widetilde{\boldsymbol{v}}_{k+1}^{*} \simeq \widetilde{\boldsymbol{R}}^{*} \, \widetilde{\boldsymbol{v}}_{k}^{*} \quad \text{for } k = 1, \ldots, K - d.$$

The *reduced-modified Koopman matrix* $\widetilde{\boldsymbol{R}}^{*}$ is an $\widetilde{N} \times \widetilde{N}$ matrix, which is computed via the pseudoinverse applied to the overdetermined system of linear equations (2.14). Once the matrix $\widetilde{\boldsymbol{R}}^{*}$ has been computed, its eigenvalues and conveniently normalized (e.g., to exhibit unit RMS norm) eigenvectors, $\mu_1, \ldots, \mu_{\widetilde{N}}$ and $\widetilde{\boldsymbol{u}}_1^{*}, \ldots, \widetilde{\boldsymbol{u}}_{\widetilde{N}}^{*}$, respectively, in conjunction with (2.14), lead to the following approximation of the reduced-modified snapshots:

$$(2.15) \qquad \widetilde{\boldsymbol{v}}_{k}^{*} \simeq \sum_{n=1}^{\widetilde{N}} \widetilde{a}_{n}^{*} \widetilde{\boldsymbol{u}}_{n}^{*} e^{(\delta_n + \mathrm{i}\,\omega_n)\,t_k},$$

where

$$(2.16) \qquad \delta_n + \mathrm{i}\,\omega_n = \frac{1}{\Delta t} \log \mu_n,$$

with the temporal distance between snapshots, Δt, as defined in (2.4).

4. *Computation of the expansion* (2.6). Premultiplying (2.15) by $\widetilde{\boldsymbol{U}}$ and invoking (2.13) lead to the counterpart of (2.15) for the reduced-modified snapshots, as

$$(2.17) \qquad \widetilde{\boldsymbol{v}}_{k} = \sum_{n=1}^{\widetilde{N}} \widetilde{a}_{n}^{*} \widetilde{\boldsymbol{u}}_{n} e^{(\delta_n + \mathrm{i}\,\omega_n) t_k},$$

where

$$(2.18) \qquad \widetilde{\boldsymbol{u}}_{n} = \widetilde{\boldsymbol{U}} \, \widetilde{\boldsymbol{u}}_{n}^{*}.$$

Now, invoking (2.10), the first J' elements in the expansion (2.17) give the counterpart of this expansion for the reduced snapshots, namely

$$(2.19) \qquad \widehat{\boldsymbol{v}}_{k} = \sum_{n=1}^{\widetilde{N}} \widehat{a}_{n} \widehat{\boldsymbol{u}}_{n} e^{(\delta_n + \mathrm{i}\,\omega_n)\,t_k},$$

where the reduced modes $\widehat{\boldsymbol{u}}_{n}$ are obtained retaining the first J' components in $\widehat{\boldsymbol{u}}_{n}^{*}$, and rescaling the resulting modes to exhibit unit RMS norm. The reduced mode amplitudes $\widehat{a}_{n}$ are calculated via least squares fitting between the left- and right-hand sides of (2.19) using the reduced snapshots $\widehat{\boldsymbol{v}}_{k}$ computed in step 1. In addition, the expansion (2.19) is truncated retaining in the right-hand side only those modes such that

$$(2.20) \qquad \frac{\widehat{a}_{n}}{\widehat{a}_{\max}} \geq \varepsilon_2,$$

where ε_2 is a tunable threshold and $\widehat{a}_{\max}$ is the maximum value of the reduced mode amplitudes. This defines the number of modes to be retained in (2.19), which is such that $N \leq \widetilde{N}$. Thus, the expansion (2.19) is rewritten as

$$(2.21) \qquad \widehat{\boldsymbol{v}}_k = \sum_{n=1}^{N} \widehat{a}_n \widehat{\boldsymbol{u}}_n \mathrm{e}^{(\delta_n + \mathrm{i}\,\omega_n)\,t_k}.$$

Finally, premultiplying the expansion (2.21) by the matrix $\boldsymbol{U}$ appearing in (2.8) leads to the expansion (2.6), where the modes and the amplitudes are given by

$$(2.22) \qquad \boldsymbol{u}_n = \frac{\widehat{a}_n}{a_n}\,\boldsymbol{U}\,\widehat{\boldsymbol{u}}$$

and

$$(2.23) \qquad a_n = \frac{|\widehat{a}_n|}{\sqrt{J}}\,\|\boldsymbol{U}\,\widehat{\boldsymbol{u}}\|_2.$$

Here, as above, J is the number of grid points and $\|\cdot\|_2$ denotes Euclidean norm. Note that the amplitudes a_n are real and ≥ 0 and the modes exhibit unit RMS norm.

As defined above, the growth rates and frequencies, δ_n and ω_n, are precisely those computed in step 3 and their number, N, coincides with the spectral complexity of the computed expansion, which generally increases as the index d is increased. On the other hand, the spatial complexity of the computed expansion is J' for all d. Therefore, taking appropriate $d > 1$ generally increases the spectral complexity, which permits dealing with cases in which the spectral complexity is larger than the spatial complexity, as anticipated.

We insist that the truncated expansions considered above are only approximations of the actual dynamics. The error of this approximation will be measured in terms of the *relative RMS error*, defined for the discrete approximations as we did in (2.9), namely

$$(2.24) \qquad \text{RRMS error} = \frac{\|\mathbf{A}_{\mathrm{approx.}} - \mathbf{A}_{\mathrm{exact}}\|_{\mathrm{Fro}}}{\|\mathbf{A}_{\mathrm{exact}}\|_{\mathrm{Fro}}},$$

where $\mathbf{A}_{\mathrm{approx.}}$ denotes the snapshot matrix approximated by the method and, as above, the norm $\|\cdot\|_{\mathrm{Fro}}$ is the Frobenius norm.

As described, the HODMD method depends on three tunable parameters, namely the dimension reduction and mode truncation thresholds, ε_1 and ε_2, respectively, and the index d. The threshold ε_1 should be chosen somewhat larger than the relative RMS accuracy of the numerical solver, and ε_2 as comparable to the relative RMS accuracy that is sought. In the applications below, the relative RMS error of the HODMD reconstruction, as defined in (2.24), will be intended to be $\sim 10^{-3}$. The index d will be selected to somewhat minimize the relative RMS reconstruction error. Let us anticipate here that the selection of d is not critical. In other words, the plot of the relative RMS error versus d is fairly flat near the minimum.

Concerning the temporal gap between consecutive snapshots, Δt, and the timespan in which the method will be applied (which is $(K-1)\,\Delta t$, where K is the number of snapshots) we consider the following:

- In order to avoid aliasing [33], Δt must be small (i.e., four or five times smaller) compared to the smallest involved period.
- In order to capture sufficient information, the timespan must be somewhat large (i.e., 1.5 times larger) than the largest involved period.

3. Binary convection in a slightly inclined cylinder. We consider the Boussinesq binary-fluid convection in a cylindrical cell of height H and radius R, slightly inclined at an angle α with respect to the horizontal. The cylinder is heated from below, with a temperature difference between the lids equal to ΔT. The whole boundary is impermeable and nonslip, with fixed temperature at the lids, while the lateral wall is assumed to be thermally insulated. We use a Cartesian coordinate system with origin at the center of the hotter lid, the z axis along the axis of the cylinder, and the x axis along the inclination direction. Thus, the gravitational acceleration is contained in the $x - z$ plane (see Figure 3.1) and given by $\mathbf{g} = g \sin \alpha \, \boldsymbol{e}_x - g \cos \alpha \, \boldsymbol{e}_z$, where $\boldsymbol{e}_x$ and $\boldsymbol{e}_z$ are unit vectors along the x and z axes, respectively. The angle α is small, meaning that the component of the gravity along the inclination of the cell is much smaller than the gravity itself.

The density varies linearly with the temperature, T, and the concentration of the denser component, C, as

$$(3.1) \qquad \rho = \rho^* \left[1 - \gamma \left(T - T^* \right) + \beta \left(C - C^* \right) \right],$$

where $\gamma > 0$ and $\beta > 0$ are the thermal and concentration expansion coefficients, respectively, T^* and C^* are the mean values of T and C, respectively, and ρ^* is the density at $T = T^*$ and $C = C^*$. The mass flux $\mathbf{J}$ for a binary mixture can be written as

$$\mathbf{J} = -\rho^* D \left[C^* \left(1 - C^* \right) S_T \nabla T + \nabla C \right],$$

where D is the mass diffusivity and S_T is the Soret coefficient. The governing equations of the problem reflect the incompressibility condition, the mass and heat conservation laws, and the Navier–Stokes equations in the Boussinesq approximation, which treats all fluid properties as constant, except for the density in the buoyancy force. They are given by

$$(3.2a) \qquad \nabla \cdot \mathbf{u} = 0,$$

$$(3.2b) \qquad \partial_t T + \left(\mathbf{u} \cdot \nabla \right) T = w \, \frac{\Delta T}{H} + \kappa \, \nabla^2 T,$$

$$(3.2c) \qquad \partial_t C + \left(\mathbf{u} \cdot \nabla \right) C = D \left[C^* \left(1 - C^* \right) S_T \nabla^2 T + \nabla^2 C \right],$$

$$(3.2d) \qquad \partial_t \mathbf{u} + \left(\mathbf{u} \cdot \nabla \right) \mathbf{u} = -\nabla \pi + \nu \, \nabla^2 \mathbf{u} + \left(-\gamma \, T + \beta \, C \right) \mathbf{g},$$

where $\mathbf{u}$ denotes the velocity field, w is its z component, π is the kinematic pressure including the gravitational contribution, κ is the thermal diffusivity, and ν is the kinematic viscosity.

In addition, we split the temperature and concentration fields, T and C, as a linear profile in z plus perturbations, Θ' and Σ', as
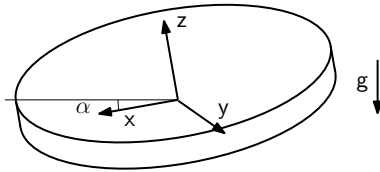

Figure 3.1. *Sketch showing the geometry of the cell and the choice of axis orientation.*

$$(3.3a) \qquad T = T^* + \Delta T \left(\frac{1}{2} - \frac{z}{H} \right) + \Theta',$$

$$(3.3b) \qquad C = C^* - C^* (1 - C^*) S_T \Delta T \left(\frac{1}{2} - \frac{z}{H} \right) + \Sigma'.$$

With this decomposition the mass flux $\mathbf{J}$ depends only on the gradient of Θ' and Σ'. Any term in the Navier–Stokes equations with a factor ρ can be split into three terms, the leading order term with only a factor ρ^*, and two terms with factors depending on T and C. If the leading order term is not a gradient, then this term is retained and the remaining two terms are neglected, while if the leading order term is a gradient, then this term is absorbed into the pressure gradient and the remaining two terms are retained.

In this paper, we present results obtained by solving numerically the nondimensional equations describing inclined binary fluid convection, which are omitted here but are discussed in detail in [14]. These equations are obtained from (3.2) by scaling lengths with the height of the cylinder H, time with the thermal diffusion time H^2/κ, temperature with ΔT, and concentration with $\Delta C = C^*(1 - C^*) S_T \Delta T$. This value of ΔC is the difference between the concentration at top and bottom lids that would appear in the quiescent state in a noninclined cylinder heated from below when the temperature difference between lids is ΔT.

The resulting system of nondimensional equations depends on the inclination angle α, the aspect ratio $\Gamma = R/H$, and four dimensionless parameters, namely the Rayleigh number Ra that provides a dimensionless measure of the vertical force imposed temperature difference ΔT, the separation ratio S that measures the ratio of the concentration contribution to the buoyancy force due to cross-diffusion, the Prandtl and Lewis numbers σ, τ, respectively, and the aspect ratio $\Gamma = R/H$. These four parameters are defined as

$$Ra = \frac{\gamma \, g \, \Delta T \, H^3}{\kappa \, \nu}, \qquad S = C^*(1 - C^*) \frac{\beta}{\gamma} S_T, \qquad \sigma = \frac{\nu}{\kappa}, \qquad \tau = \frac{D}{\kappa}.$$

The values of the dimensionless parameters used in this paper, which correspond to the binary mixture used in the experiment described in [13], will include several values of Ra and the following fixed values of the remaining parameters:

$$(3.4) \qquad \alpha = 0.024 \, \text{rad}, \quad \Gamma = 5, \quad S = 0.13, \quad \sigma = 16, \quad \tau = 0.011.$$

Notice that, since the whole boundary is impermeable ($\mathbf{J} \cdot \mathbf{n} = 0$ at the boundaries) the spatial mean value of the concentration remains constant during the temporal evolution. When using the nondimensional equations, the value of the scaled fluctuation of the concentration $\Sigma = \Sigma'/\Delta C$ has a spatial mean value $\langle \Sigma \rangle$ that is fixed by the initial condition. In these equations, the deviation of the concentration field from this spatial mean value, which will be denoted by $\tilde{\Sigma} = \Sigma - \langle \Sigma \rangle$, corresponds to the rescaled deviation of the physical concentration with respect to the spatial mean value C^* plus the linear profile.

The nondimensionalized system of equations and boundary conditions has been solved numerically using the algorithm described in [34]. To integrate the equations in time, we use the second order time-splitting method proposed in [35] combined with a pseudospectral method for the spatial discretization, Galerkin–Fourier in the azimuthal coordinate ϕ, and

Chebyshev collocation in r and z. More details about the derivation of the equations and the numerical method can be found in some previous works in the same or related configurations [14, 36, 37].

Equations and boundary conditions are equivariant under the group of symmetries G that contains the transformations $\{I, R_1^{3D}, R_2^{3D}, R_3^{3D}\}$, where I stands for the identity, R_1^{3D} is a reflection with respect to the middle longitudinal vertical plane ($y = 0$), R_2^{3D} is a point symmetry with respect to the center of the cylinder, and R_3^{3D}, which is the composition of the previous transformations, is a rotation by π about the line $x = 0$, $z = 1/2$, the diameter parallel to the y axis located in the center of the cylinder. These transformations act on the dimensionless cylindrical components of the velocity field u, v, w and deviation of the dimensionaless temperature Θ and concentration $\tilde{\Sigma}$ defined above as follows:

$$R_1^{3D} : (r, \phi, z) \to (r, -\phi, z), \qquad (u, v, w, \Theta, \tilde{\Sigma}) \to (u, -v, w, \Theta, \tilde{\Sigma}),$$
$$R_2^{3D} : (r, \phi, z) \to (r, \pi + \phi, 1 - z), \quad (u, v, w, \Theta, \tilde{\Sigma}) \to (u, v, -w, -\Theta, -\tilde{\Sigma}),$$
$$R_3^{3D} : (r, \phi, z) \to (r, \pi - \phi, 1 - z), \quad (u, v, w, \Theta, \tilde{\Sigma}) \to (u, -v, -w, -\Theta, -\tilde{\Sigma}).$$

As we shall apply the HODMD method to the temperature and concentration fields at the midheight plane of the cylindrical container $z = 1/2$, it is important to bear in mind the action of these transformations at this plane, which are

$$R_1 : (r, \phi) \to (r, -\phi), \qquad (\Theta, \tilde{\Sigma}) \to (\Theta, \tilde{\Sigma}),$$
$$R_2 : (r, \phi) \to (r, \pi + \phi), \quad (\Theta, \tilde{\Sigma}) \to (-\Theta, -\tilde{\Sigma}),$$
$$R_3 : (r, \phi) \to (r, \pi - \phi), \quad (\Theta, \tilde{\Sigma}) \to (-\Theta, -\tilde{\Sigma})$$

in polar coordinates, while in rectangular coordinates they read as

$$R_1 : (x, y) \to (x, -y), \qquad (\Theta, \tilde{\Sigma}) \to (\Theta, \tilde{\Sigma}),$$
$$R_2 : (x, y) \to (-x, -y), \quad (\Theta, \tilde{\Sigma}) \to (-\Theta, -\tilde{\Sigma}),$$
$$R_3 : (x, y) \to (-x, y), \qquad (\Theta, \tilde{\Sigma}) \to (-\Theta, -\tilde{\Sigma}).$$

Large scale steady flow. In the slightly inclined flat cylinder we are considering here, contrary to what happens in a purely horizontal container, the basic flow that arises for small heating (i.e., moderate Rayleigh number) is not a quiescent state. Instead, the basic state is an almost horizontal circulatory shear motion of the fluid layer, known as *large scale steady flow* (LSSF). The warm fluid near the lower lid of the cylinder moves uphill (to negative x), almost parallel to the lid, and, when it arrives to the lateral boundary, it moves upward generating a narrow boundary layer. Then, the fluid moves almost parallel to the upper lid downhill (to positive x), and the cooler fluid sinks downward.

The temperature and concentration distributions at the midplane, $z = 0.5$, for the present LSSF are depicted in Figure 3.2. As can be seen in plot (a), the temperature departure from the vertically linear profile is very small outside the lateral boundary layers. Plot (b) shows that, instead, the concentration field of the heavier component varies monotonously along the inclination. Also, we observe that the denser component of the mixture accumulates downhill, as expected from the Soret effect for a mixture with a positive value of the separation ratio
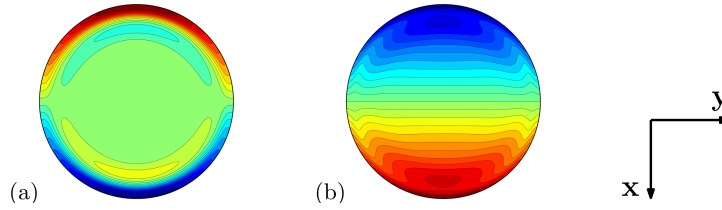
Figure 3.2. *Contours of* (a) *the temperature and* (b) *the concentration fields for the LSSF state at* $z = 0.5$ *for* $Ra = 1600$. *In these and in the remaining contour plots in the paper, the color scale for both the temperature and concentration goes from blue (for smaller values) to red (for larger values).*

S. This solution is invariant under the action of R_1^{3D}, R_2^{3D}, and R_3^{3D} considered above. Hereinafter, we call C the rescaled concentration field obtained from the numerical calculations, i.e., $C = -(\frac{1}{2} - z) + \Sigma$; then at the midplane of the cell, $z = 0.5$, the concentration is $C = \Sigma$.

4. Results: Application of HODMD to the anaylysis of SHC patterns. In the various applications of the HODMD method below, this method will be applied to the time-dependent temperature Θ and concentration of the heavier component C fields at the midplane of the cell, $z = 0.5$. When seeking attractors, we disregard transient behavior by first integrating the system along very large timespans. After this, we set $t = 0$ and begin collecting snapshots.

Consistently with the discretization used in the numerical solver, in this $x - y$ plane we use a polar coordinate system, with the radial and the azimuthal coordinates defined as $r = \sqrt{x^2 + y^2}$ and $\phi = \tan^{-1}(x/y)$, respectively. The counterparts of (2.1) and (2.3) for the temperature and concentration are

$$(4.1) \qquad \Theta(r, \phi, t) = \sum_{n=1}^{N} a_n^{\Theta} \Theta_n(r, \phi)\, e^{(\delta_n + i\,\omega_n)\,t},$$

$$(4.2) \qquad C(r, \phi, t) = \sum_{n=1}^{N} a_n^{C} C_n(r, \phi)\, e^{(\delta_n + i\,\omega_n)\,t},$$

and

$$(4.3) \qquad \Theta(r_{i_1}, \phi_{i_2}, t_k) = \sum_{n=1}^{N} a_n^{\Theta} \Theta_n(r_{i_1}, \phi_{i_2})\, e^{(\delta_n + i\,\omega_n)\,t_k},$$

$$(4.4) \qquad C(r_{i_1}, \phi_{i_2}, t_k) = \sum_{n=1}^{N} a_n^{C} C_n(r_{i_1}, \phi_{i_2})\, e^{(\delta_n + i\,\omega_n)\,t_k},$$

respectively. In the expansions (4.1)–(4.4), the amplitudes and modes are different for the temperature and concentration, but the growth rates and frequencies, δ_n and ω_n, respectively, coincide for both fields with great precision, in spite of the fact that the HODMD method is applied separately to the temperature and concentration fields. The discretized expansions (4.3) and (4.4) will be obtained using $I_1 = 101$ Chebyshev collocation points in the radial direction and $I_2 = 150$ equispaced points in the azimuthal coordinate. The thermal and concentration modes will be normalized such that they exhibit unit RMS norm, namely

$$(4.5) \qquad \frac{\|\Theta_n\|_2}{\sqrt{I_1 I_2}} = \frac{\|C_n\|_2}{\sqrt{I_1 I_2}} = 1,$$

where $\|\cdot\|_2$ denotes the usual Euclidean norm, as in (2.23).

4.1. Symmetric superhighway convection at $Ra = 1610$. As anticipated, there are several branches of symmetric SHC states, i.e., the temperature field shows objects that are aligned along the inclination direction in approximately parallel lanes and counterpropagate periodically in adjacent lanes. These states differ from each other in the spatio-temporal symmetries they exhibit.

To be explicit, if we denote a solution by $\Psi(r, \phi, z, t) = (u, v, w, \Theta, \Sigma)$,

- type I symmetric SHC has the spatio-temporal symmetry

$$R_2^{3D}\Psi(r, \phi, z, t) = \Psi(r, \phi, z, t + T/2),$$

- type II symmetric SHC has the spatio-temporal symmetry

$$R_1^{3D}\Psi(r, \phi, z, t) = \Psi(r, \phi, z, t + T/2),$$

- type III symmetric SHC is a periodic R_2^{3D} invariant state

$$R_2^{3D}\Psi(r, \phi, z, t) = \Psi(r, \phi, z, t),$$

- type IV symmetric SHC is a periodic R_1^{3D} invariant state

$$R_1^{3D}\Psi(r, \phi, z, t) = \Psi(r, \phi, z, t).$$

Although there are four types of these solutions, we focus on the stable type I SHC that we have obtained for $Ra = 1610$ and the mentioned value of the physical and geometric parameters (3.4). The period of this periodic SHC is $T = 2\pi/\omega_1 \simeq 4.166$, where the fundamental frequency $\omega_1 = 1.5082$ will be calculated below. The evolution of the temperature and concentration at a representative interior point at mid height is given in Figure 4.1. As can be seen, the temperature shows an almost monochromatic oscillation around its mean value, and the concentration exhibits a less monochromatic oscillation. These statements will be confirmed below.
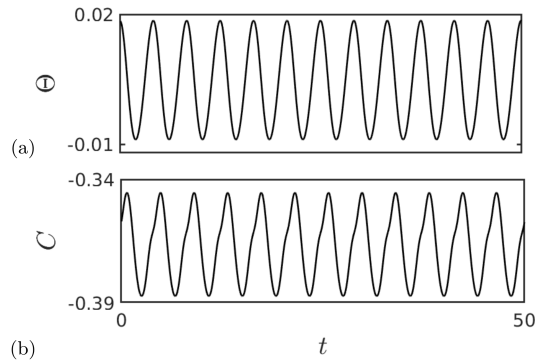

Figure 4.1. *Temporal evolution of* (a) *temperature Θ and* (b) *concentration C at the mid-height point $r = R/2, \phi = 45°$, in nondimensional units, for the type I SHC oscillation that is obtained for $Ra = 1610$.*
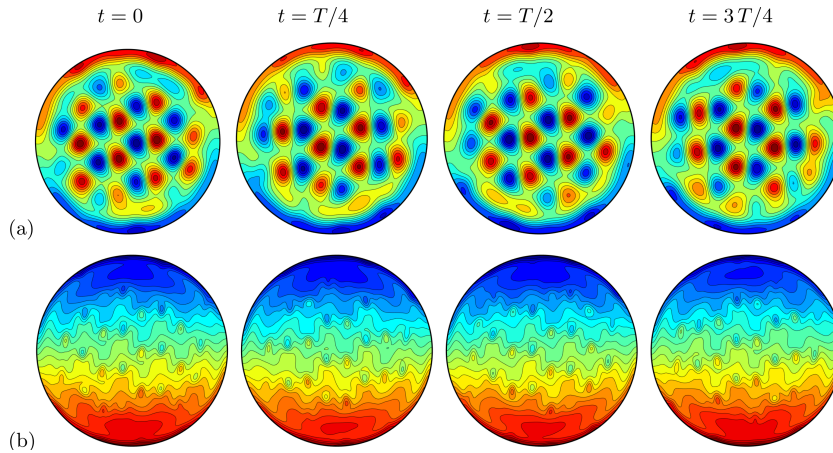
Figure 4.2. *Type* I *SHC oscillation obtained for Ra* = 1610*: contour plots of* (a) Θ *and* (b) C *at the midplane of the cylinder for four equispaced snapshots along a cycle of the SHC state obtained by numerical simulation at Ra* = 1610.

Several representative snapshots along one oscillation cycle, $0 \leq t \leq T$, are given in Figure 4.2. As can be seen in plot (a), the temperature field exhibits a well-defined (super-highway) pattern, in which roughly round spots counterpropagate along eight well-defined, almost vertical lines in the plots, namely along the direction of inclination of the cylinder (x axis). The red spots (which are hotter) move uphill and the colder blue spots move downhill. Superposed to that displacement, the spots exhibit a slight lateral oscillation (y axis), giving rise to a global zig-zag motion [14]. In addition, a boundary layer is also seen in this figure, where the fluid is hot in the upper side of the figure and cold in the lower side. The concentration field considered in plot (b), instead, exhibits a much less defined structure, in which the concentration is smaller in the upper side and larger in the lower side of the cylinder. The dynamics for the concentration appears to be fairly irregular, which is intriguing because the (temporal) dynamics is strictly periodic. In fact, we can only observe in the pattern the presence of small bubble-like localized structures, which counterpropagate along the same eight vertical lines that are observed for the temperature. The blue/lighter bubbles are located near the red spots of temperature and travel uphill, while the red/denser bubbles are located near the blue spots of temperature and travel downhill.

Notice how the symmetry $R_2^{3D}\Psi(r,\phi,z,t) = \Psi(r,\phi,z,t+T/2)$ can be easily appreciated through a close look of the snapshots plotted in Figure 4.2. For example, the snapshots at the midplane of the temperature field at $t = 0$ and $t = T/2$ satisfy $\Theta(r,\phi+\pi,t) = -\Theta(r,\phi,t+T/2)$, in agreement with the symmetry of the solution. In this plane, the mean value of temperature Θ is zero, and that of concentration is $\bar{C}_0$.

Let us now apply the HODMD method to this type of solution, discussing the information provided by this type of decomposition. In the application of the method, we take the following values of the tunable parameters, namely the index d and the dimension reduction and mode truncation thresholds, ε_1 and ε_2, respectively:

$$(4.6) \qquad\qquad 1 \leq d \leq 10, \quad \varepsilon_1 = 10^{-5}, \quad \varepsilon_2 = 10^{-3}.$$

The number of snapshots is 50 in the time interval $0 \leq t \leq 5$, which is slightly larger than the period of the cycle (see Figure 4.1). Note that the index d is taken in a wide interval, obtaining essentially the same results, which illustrates the robustness of the method. Also, the value $d = 1$ already gives very good results, which is due to the fact that the spatial and spectral complexities coincide in the present case. Since the data are taken in the attractor, the values of the growth rates δ_n in the expansions (4.1)–(4.2) are both very small (namely, $|\delta_n| \leq 10^{-5}$ for both the temperature and concentration) and we concentrate only on the frequencies ω_n. The relative RMS reconstruction error, according to (2.24), is $\sim 1.6 \cdot 10^{-4}$ for the temperature field and $\sim 4 \cdot 10^{-4}$ for the concentration field, retaining seven modes in both cases, which exhibit the same values of the frequencies with great precision (five significant digits). It must be noted that the numbers of modes retained for reconstructing the temperature and concentration fields do not generally coincide because these fields are treated separately by the HODMD method. However, these numbers of modes do coincide in the present case.

The relevant amplitude versus frequency ($a - \omega$) diagrams for the temperature and concentration fields are given in Figure 4.3, where it can be seen that the amplitudes decay spectrally for both the temperature and concentration. This would be more clearly seen if higher order harmonics were considered in this plot (by decreasing the value of the mode truncation threshold, ε_2; see (4.6)), which is not done here for the sake of brevity. Also, the expansions for both the temperature and concentration contain a (real) mode with $\omega = 0$, which corresponds to the temporal mean fields, and three pairs of complex conjugate modes with $\omega_n \neq 0$, which give the oscillations around the mean fields. The ratio of the amplitudes of the dominant oscillatory modes to the next oscillatory modes is larger than 10 for the temperature and much smaller for the concentration. This explains that, as anticipated, the temperature oscillations are more monochromatic than the oscillations of the concentration. On the other hand, the amplitude of the mean field mode is comparable to (though somewhat larger than) that of the dominant oscillatory modes for the temperature, but it is 55 times larger for the concentration, which means that the mean field mode dominates the spatio-temporal concentration field. In other words, the mean field mode, which as seen below is very irregular, masks any possible (regular) pattern in the oscillatory concentration field.

It turns out that for both the temperature and concentration, the relevant frequencies, with a precision of five significant digits, are $\omega_1 = 1.5082$ and its (positive and negative) harmonics. Thus, ignoring the growth rates (which as anticipated are very small in the present case), the expansions (4.1)–(4.2) can be rewritten as
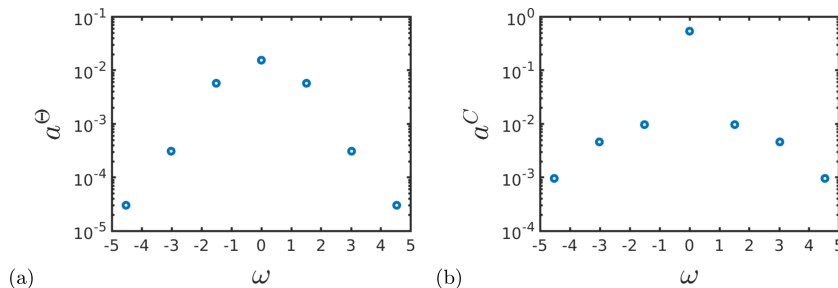

(a) ω (b) ω

Figure 4.3. *Type* I *SHC oscillation for Ra $=$ 1610: $a - \omega$ diagrams for the* (a) *temperature and* (b) *concentration fields in the application of the HODMD method to the SHC state.*

$$(4.7) \qquad \Theta(r,\phi,t) = \sum_{n=-3}^{3} a_n^{\Theta} \Theta_n(r,\phi) \, \mathrm{e}^{\mathrm{i}\,n\,\omega_1 t}, \quad C(r,\phi,t) = \sum_{n=-3}^{3} a_n^{C} C_n(r,\phi) \, \mathrm{e}^{\mathrm{i}\,n\,\omega_1 t}.$$

Since the left-hand sides in these expansions are real, the mean field modes, Θ_0 and C_0, are real, and the remaining oscillatory modes appear in complex conjugate pairs, namely $\Theta_n = \overline{\Theta}_{-n}$ and $C_n = \overline{C}_{-n}$, for $n = 1, 2$, and 3.

Figure 4.4 shows the various modes in the expansions for the temperature and concentration appearing in the expansions (4.7), plotting the spatio-temporal mean field modes, which are real, and the real and imaginary parts of the three oscillatory modes associated with
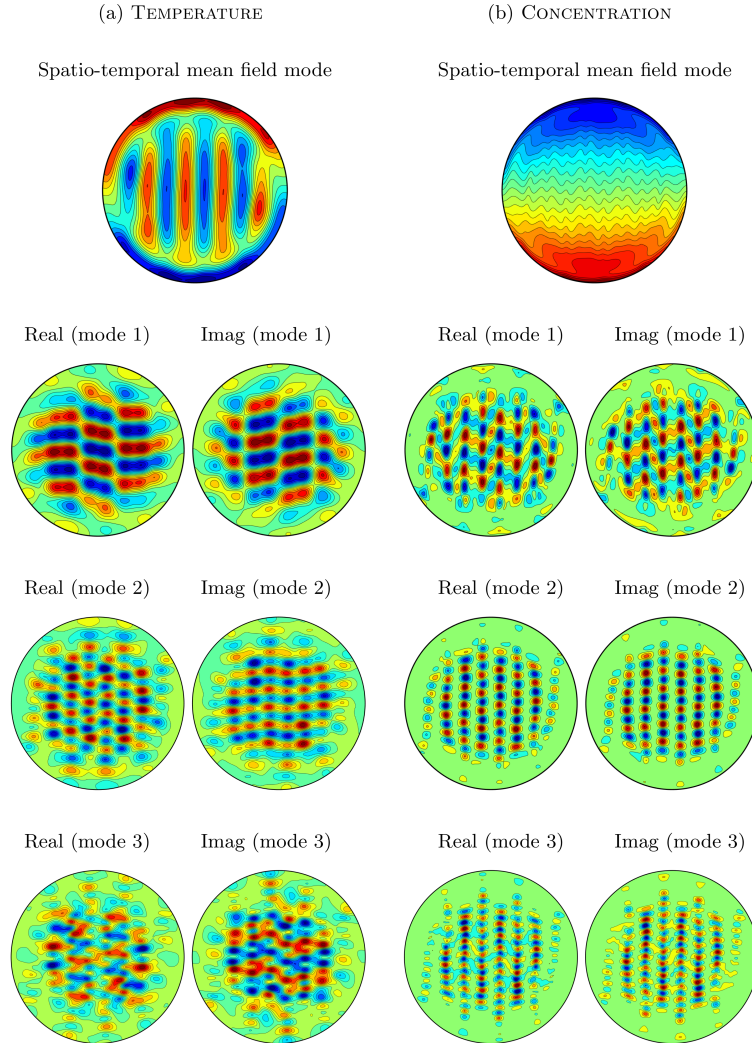

Figure 4.4. *Type* I *SHC oscillation obtained for Ra= 1610: contours of* (a) *the temperature and* (b) *concentration modes appearing in* (4.7) *associated with the spatio-temporal mean field* ($\omega = 0$)*, and the real and imaginary parts of the modes associated with the positive frequencies* $\omega = \omega_1$ *(mode 1),* $\omega = 2\,\omega_1$ *(mode 2), and* $\omega = 3\,\omega_1$ *(mode 3).*

the positive frequencies ω_1, $2\,\omega_1$, and $3\,\omega_1$, which are called mode 1, mode 2, and mode 3, respectively.

Some relevant features concerning the modes for the temperature, plotted in Figure 4.4(a), are as follows:

- The spatio-temporal mean field mode shows approximately vertical (i.e., almost aligned with the inclination direction) blue and red stripes at horizontal positions that, more or less, coincide with the horizontal positions of the vertical lanes of the SHC pattern, considered in Figure 4.2(a). Thus, the spatial structure of the spatio-temporal mean field mode for the temperature in this SHC pattern resembles that of a longitudinal-roll pattern, rather than that of the LSF flow, plotted in Figure 3.2.
- The oscillatory mode 1 shows, approximately, transversal patterns that will give rise to an oscillatory pattern between the real and imaginary parts of this mode. The vertical lanes observed in the SHC solution plotted in Figure 4.2(a) cannot be easily identified in the spatial structure of this mode. In other words, the number of objects in each vertical line of this mode essentially doubles its counterpart in the SHC solution. Moreover, while the objects in each lane in Figure 4.2(a) are all of the same color (either blue or red), namely they all correspond to either low or high temperature, the objects along each line in Figure 4.4(a) for mode 1 alternates between blue and red. As explained below, this color change has to do with the mean field mode, which contributes to the SHC solution, but is absent in the oscillatory mode 1.
- In the oscillatory mode 2 (which, according to Figure 4.3, exhibits a much smaller amplitude than that of mode 1), the vertical wavenumber doubles and gives rise to much smaller structures. In this case, the vertical lanes structure of the SHC solution (see Figure 4.2(a)) is easily observed. In this mode, though, warm and cold spots alternate in each vertical line, while they are of the same color in each vertical lane of the SHC pattern. The horizontal position of the vertical lines in this mode 2 barely varies in the real and imaginary parts of the mode.
- The oscillatory mode 3 exhibits a still much smaller amplitude (see Figure 4.3) and it has a very small effect on the SHC pattern plotted in Figure 4.2(a).

Concerning the modes for the concentration plotted in Figure 4.4(b), they show the following relevant features:

- The spatio-temporal mean field mode is very irregular. Also, the contour plots of this mode closely resemble/look like those of the LSF solution in Figure 3.2, except that the very smooth almost-horizontal contour lines in the LSF are replaced here by wavy contour lines.
- In the oscillatory mode 1, the fixed vertical lanes structure of the SHC solution can be appreciated. Note that, in this mode, heavier and lighter spots alternate along each line.
- As in mode 2 for the temperature, the vertical wavenumber is doubled in the oscillatory mode 2 for the concentration and the number of smaller structures doubles. The vertical lines in this mode are located at the same horizontal positions as in mode 1.
- As happened with the temperature, the amplitude of mode 3 is very small and, thus, it has a very small effect on the SHC pattern plotted in Figure 4.2(b).

Once the spatial modes, amplitudes, growth rates, and frequencies provided by the HODMD method are available, it is possible to reconstruct relevant approximations of the temperature and concentration fields using proper truncations in the expansions (4.7).

Beginning with the temperature, we consider two monochromatic reconstructions by either (i) considering only the effect of mode 1 and its complex conjugate (i.e., those modes associated with the frequencies $\pm\omega_1$), namely

$$(4.8) \qquad \Theta(r,\phi,t) = a_1^\Theta \Theta_1(r,\phi) \, \mathrm{e}^{\mathrm{i}\,\omega_1\,t} + c.c.,$$

where $c.c.$ denotes hereinafter the complex conjugate, and (ii) adding the mean field to the effect of mode 1 and its complex conjugate, namely

$$(4.9) \qquad \Theta(r,\phi,t) = [a_1^\Theta \, \Theta_1(r,\phi) \, \mathrm{e}^{\mathrm{i}\,\omega_1\,t} + c.c.] + a_0^\Theta \, \Theta_0(r,\phi).$$

Figure 4.5 illustrates some properties of the monochromatic reconstructions (4.8) and (4.9). As can be seen in plot (a), the spatio-temporal pattern for the reconstruction (4.8) exhibits an
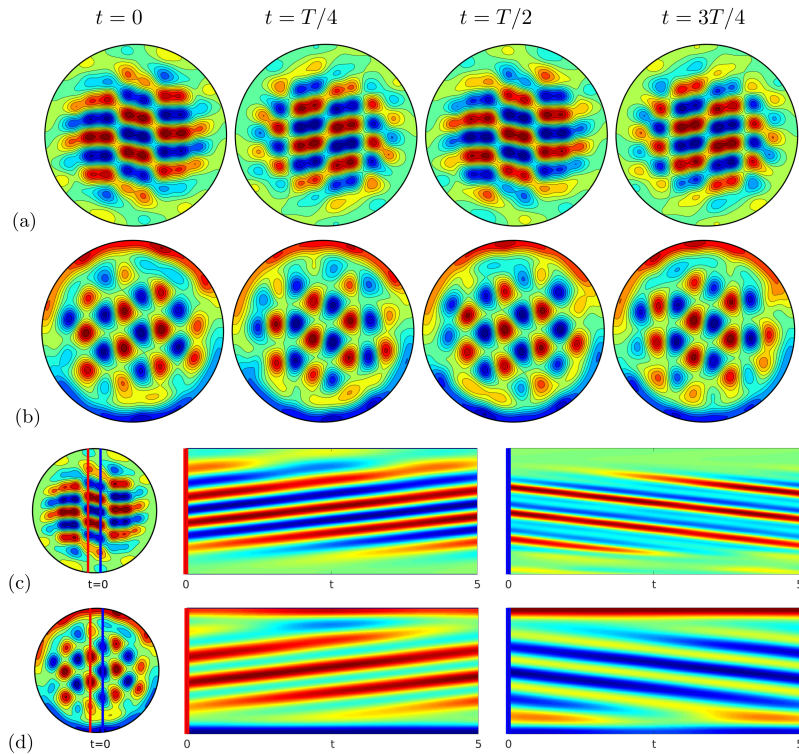

Figure 4.5. *Type* I *SHC oscillation obtained for Ra= 1610: temperature contours along a cycle, considering four temporally equispaced snapshots, of two monochromatic reconstructions in the SHC state, showing* (a) *the dynamics associated with* (4.8), *and* (b) *the counterpart of plot* (a) *considering the dynamics displayed in* (4.9). (c) *For the monochromatic reconstructed dynamics associated with* (4.8), *the temperature contours at* $t = 0$ *(left plot) and the space-time plots (middle and right plots) showing the evolution of* Θ *along the two off-diameter (middle-red and right-blue) vertical red and blue lines depicted in the left contour plot.* (d) *Counterpart of* (c) *for the reconstruction displayed in* (4.9). *A video showing the continuous temporal evolution associated with plots* (a) *and* (b) *can be found in the Supplementary Materials,* M144741_01.mp4 *[local/web 1206MB], to this paper.*

almost horizontal pendular motion, in which the structures reorder and split themselves in the transversal direction during the oscillation. Apparently, this motion is completely different from the actual SHC pattern considered in Figure 4.2(a). However, plot (b) shows that if the mean field mode is added to the former oscillation, then the resulting snapshots do match qualitatively those corresponding to the SHC pattern plotted in Figure 4.2(a).

In order to understand how the superposition of the oscillatory pattern (4.8) and the steady mode associated with the mean field, which gives the pattern (4.9), resembles qualitatively the SHC pattern, we need to gain insight into the actual dynamics along two vertical lines for both patterns, namely (4.8) and (4.9). In particular, by plotting the temperature space-time diagrams for the pattern (4.8) in two parallel off-diameter lines (i.e., the two vertical red and blue lines indicated in Figure 4.5(c), left) along the direction of inclination, we are able to see the evolution of the temperature with time along these lines. We observe that the warm (red) and cold (blue) spots in these vertical lines do indeed travel along the direction of inclination. In the case of the spots over the red line, the locations of both the warmer and cooler spots correspond to ascending and descending (along the z-direction) fluid, respectively. The spots in the red line form waves traveling uphill (Figure 4.5(c), middle), while in the case of the spots over the blue line, the location of both the warmer and cooler regions of fluid form a wave traveling downhill (Figure 4.5(c), right). On the other hand, in the longitudinal roll pattern associated to the mean field (Figure 4.4(a), top), points over the red line fit the red part of the roll, that is, the region of warmer ascending fluid, while points over the blue line fit the blue part of the roll, that is, the region of cooler descending fluid. Thus, when the mean field is added to the dominant monochromatic oscillation (i.e., when the reconstruction (4.9) is considered), then over the red line, the warmer spots are reinforced, whereas the colder spots almost vanish (green-yellow), and over the blue line, the cooler spots are reinforced, whereas the warmer spots almost vanish (green-yellow). This simple mechanism generates the SHC pattern, with only warm spots traveling uphill and only cold spots traveling downhill in alternating lanes, as can be seen in Figure 4.5(d).

Let us mention here that the approximation (4.9), which only retains the mean field and the dominant oscillatory modes associated with $\omega = \pm\omega_1$, gives a fairly good approximation of the thermal field in the SHC pattern even quantitatively. This is because, as seen in Figure 4.3(a), the amplitudes of the neglected modes are more than one order of magnitude smaller than those of the retained modes.

Concerning the concentration pattern, Figure 4.3(b) shows that the amplitudes of the $\omega = \pm 2\,\omega_1$-modes are not so small for the concentration, whose description requires retaining these modes. On the other hand, for the concentration, the amplitude of the steady mean field mode is 60 times larger than that of the dominant oscillatory modes, associated with $\omega = \pm\omega_1$. Thus, the mean field mode masks the remaining oscillatory modes in the SHC pattern for the concentration, and we shall analyze the time-dependent reconstruction of the concentration without including the mean field. In other words, we shall consider two type of patterns, either retaining the modes associated with $\omega = \pm\omega_1$ only, namely (cf. (4.8)–(4.9))

$$(4.10) \qquad\qquad C(r,\phi,t) = a_1^C\, C_1(r,\phi)\, e^{i\,\omega_1\,t} + c.c.,$$

or retaining also the two modes associated with $\omega = \pm 2\,\omega_1$, namely

$$(4.11) \qquad C(r,\phi,t) = a_1^C\, C_1(r,\phi)\, e^{i\,\omega_1\,t} + a_2^C\, C_2(r,\phi)\, e^{2\,i\,\omega_1\,t} + c.c.$$

The counterpart of Figure 4.5 for the patterns (4.10) and (4.11) is given in Figure 4.6. In particular, Figure 4.6(a) considers the concentration contour plots for the monochromatic dynamics (4.10), constructed as the superposition of the modes associated with the frequencies $\omega = \pm\omega_1$ at four time instants along a cycle of the SHC state. As can be seen, the structure of this concentration pattern shows eight vertical parallel lines that very approximately correspond to the lines in the SHC thermal pattern. The number of objects in each vertical line essentially doubles its counterpart in Figure 4.2(a) and also doubles the number of small bubbles observed in Figure 4.2(b). As it happened with the temperature field, when only the modes associated with the frequencies $\omega = \pm\omega_1$ are retained, then the objects within each line in Figure 4.6(a) alternate between blue and red (namely, between low and high concentration). On the other hand, if we reconstruct the concentration field as in (4.11), namely by retaining the modes associated with the frequencies $\omega = \pm\omega_1$ and $\omega = \pm2\,\omega_1$, then we
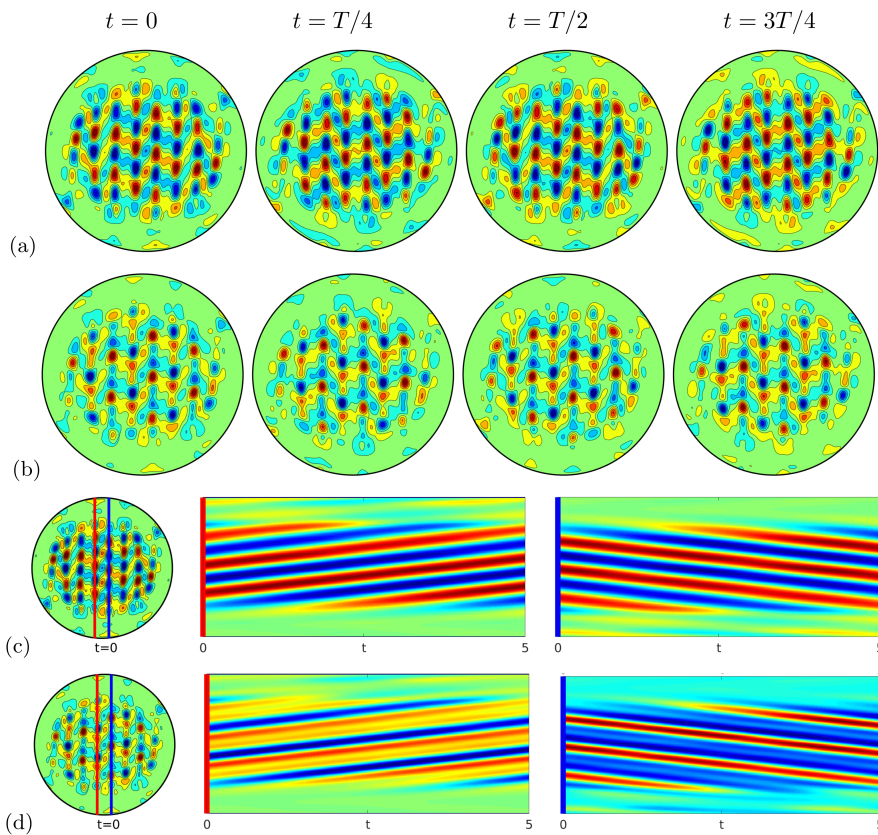

Figure 4.6. *Type* I *SHC oscillation obtained for Ra* = 1610: *concentration contours along a cycle of the SHC state showing* (a) *the monochromatic dynamics associated with* (4.10) *for four equispaced snapshots along a cycle and* (b) *the counterpart of plot* (a) *as obtained by considering the monochromatic reconstruction defined in* (4.11). (c) *For the reconstructed pattern displayed in* (4.10), *the concentration contour at* $t = 0$ *(left) and the space-time plots showing the evolution of C along the two off-diameter (left red and right blue) vertical lines depicted in the contour plot.* (d) *Counterpart of plot* (c), *but considering the pattern defined in* (4.11). *A video showing the continuous temporal evolution associated with plots* (a) *and* (b) *can be found in the Supplementary Materials,* M144741_02.mp4 *[local/web 1589MB], to this paper.*

observe in Figure 4.5(b) the same eight vertical parallel lines appearing in Figure 4.6(a), with the same number of objects in each line, but now in each line either red or blue bubbles are reinforced or diminished, depending on the line.

As we did for the temperature, in order to understand how the superposition of the modes associated with the frequencies $\pm\omega_1$ and $\pm 2\,\omega_1$ gives rise, very approximately, to the oscillatory SHC pattern, we need to gain insight into the actual dynamics along vertical lines in the pattern. In particular, by plotting the concentration space-time plots for the monochromatic dynamics obtained by superposition of the $\pm\omega_1$ modes in two parallel off-diameter lines along the direction of inclination (Figure 4.6(c)), we observe that, as happened with temperature, both the light and dense spots in each vertical line travel along the direction of inclination. The spots over the red line on the left (that is, the location of both the lighter and denser regions of fluid) form a wave traveling uphill (Figure 4.6(c), middle), and the spots over the blue line (that is, the location of both the lighter and denser regions of fluid) form a wave traveling downhill (Figure 4.6(c), right). Although not shown here, the same behavior is observed in the monochromatic reconstruction retaining the $\pm 2\,\omega_1$ modes only, but in this case the number of red and blue spots along the vertical lines doubles those for the $\pm\omega_1$ monochromatic oscillation. As a result, when the two patterns are added up, namely when the modes $\pm\omega_1$ and $\pm 2\,\omega_1$ are retained (Figure 4.6(d)), the blue spots over the red line are reinforced and form the small uphill-traveling blue bubbles (Figure 4.6(d), middle), while the red spots over the blue line are reinforced and form the small downhill-traveling red bubbles (Figure 4.6(d), right). It is interesting to note that this spatio-temporal pattern for the concentration was not clearly observed in Figure 4.2(b) because, there, it was masked by the mean field. However, it is worth mentioning that, when we subtract the mean concentration field (which could also be obtained by averaging over a period the numerical solution) from the full nonlinear periodic concentration field obtained by numerical simulation we obtain a periodic pattern that very approximately matches the reconstructed solution obtained by retaining the $\pm\omega_1$ and $\pm 2\,\omega_1$ modes (Figure 4.6(d)).

It is interesting to note that the results above (in particular, the expansions (4.3) and (4.4), which apply in the whole spatial domain) have been obtained with great precision using data in a timespan that is only slightly larger than the oscillation period. These are great advantages of the HODMD method comparing with the performance of more classical methods, such as FFT or power spectral density [38]. These advantages are even more evident in the more complex dynamics considered in the next subsection.

Concerning the spatial symmetries, the quantitative inspection of the Θ_n and C_n modes appearing in (4.7) shows that these exhibit the following reflection symmetry, with an accuracy of three significant digits:

$$(4.12) \qquad \Theta_n(r, \phi + \pi) = -\Theta_n(r, \phi), \quad C_n(r, \phi + \pi) = -C_n(r, \phi) \text{ if } 0 \neq n = \text{even}$$

and

$$(4.13) \qquad \Theta_n(r, \phi + \pi) = \Theta_n(r, \phi), \quad C_n(r, \phi + \pi) = C_n(r, \phi) \text{ if } n = \text{odd}.$$

The satisfaction of this symmetry can also be appreciated in the contour plots depicted in Figure 4.4.

Let us remark here that even though $n = 0$ can be considered as even, the symmetry (4.13) applies with the same accuracy to Θ_0 but it does not apply to C_0. This is because this symmetry can apply only if the mode exhibits zero spatial mean value. The spatial mean values of Θ_0 and C_0 are not zero, but turn out to be

$$(4.14) \qquad \Theta_0^{\mathrm{mean}} = 4.4 \cdot 10^{-6}, \quad C_0^{\mathrm{mean}} = -0.93.$$

Note that Θ_0^{mean} is very small but C_0^{mean} is not.

If we subtract C_0^{mean} from the temporal mean field mode, C_0, we obtain the *spatio-temporal mean field mode*, which is given by

$$(4.15) \qquad C_0^{\mathrm{STMFM}} = C_0 - C_0^{\mathrm{mean}}.$$

To the approximation relevant here, Θ_0 and C_0^{STMFM} do satisfy the symmetry (4.12), namely

$$(4.16) \qquad \Theta_0(r, \phi + \pi) = -\Theta_0(r, \phi), \quad C_0^{\mathrm{STMFM}}(r, \phi + \pi) = -C_0^{\mathrm{STMFM}}(r, \phi).$$

On the other hand, multiplying C_0^{mean} by a_0^C, we obtain

$$(4.17) \qquad C^{\mathrm{STmean}} \equiv a_0^C C_0^{\mathrm{mean}} \simeq -0.5,$$

which can be considered as the *spatio-temporal mean* of the concentration along the attractor.

For a three-dimensional (3D) solution with the spatio-temporal symmetry described before, the mean value of the fluctuation of the temperature Θ of the temporal mean field at the midplane must be zero. If we calculate the value $\Theta_0^{\mathrm{STmean}} \equiv a_0^\Theta \Theta_0^{\mathrm{mean}}$, we obtain a very small value ($\simeq 6.85 \cdot 10^{-8}$) compared with the values of the temperature ($\simeq 10^{-2}$) of the mean field. This small value can be attributed to the decimal truncation of the formatted data used in the aplication of the HODMD method. The origin of the mean value of the concentration of the mean field mode is different. As we have mentioned before, the concentration field in the 3D solution may have a mean value $\langle \Sigma \rangle$ that is fixed from the intial condition of the concentration field in the numerical time evolution. Thus, the mean value of the temporal mean field mode at the midplane may have a value significantly different from zero. For a 3D solution with the spatio-temporal symmetry described before, the value of C^{STmean} should be equal to $\langle \Sigma \rangle$.

Using (4.15)–(4.17), the expansions (4.7) can be rewritten as

$$(4.18) \qquad \Theta(r, \phi, t) = a_0^\Theta \Theta_0(r, \phi) + \left[\sum_{n=1}^{3} a_n^\Theta \Theta_n(r, \phi) \, e^{i n \omega_1 t} + c.c. \right],$$

$$(4.19) \qquad C(r, \phi, t) = C^{\mathrm{STmean}} + a_0^C C_0^{\mathrm{STMFM}}(r, \phi) + \left[\sum_{n=1}^{3} a_n^C C_n(r, \phi) \, e^{i n \omega_1 t} + c.c. \right].$$

Recalling that the period of the oscillation is $T = 2\pi/\omega_1$ (which means that $n\omega_1 T/2 = n\pi$) and noting that $e^{i n \pi} = 1$ and -1 for $n = $ even and odd, respectively, (4.12)–(4.13), (4.16), and (4.18)–(4.19) imply that, to the approximation relevant here, the temperature and concentration fields exhibit, as expected, the spatio-temporal reflection symmetry

$$\Theta(r, \phi + \pi, t) = -\Theta(r, \phi, t + T/2),$$
$$(4.20) \qquad C(r, \phi + \pi, t) - C^{\mathrm{STmean}} = -\left[C(r, \phi, t + T/2) - C^{\mathrm{STmean}} \right],$$

which can also be written as

$$x \to -x, \quad y \to -y, \quad t \to t + T/2,$$

(4.21)
$$\Theta \to -\Theta, \quad C - C^{\mathrm{STmean}} \to -\left(C - C^{\mathrm{STmean}}\right).$$

It is to be noted that, under the symmetry defined in (4.20) or (4.21), the mid diameter along the direction of inclination is just in between two counterpropagating lanes of the SHC, which means that the number of lanes in this pattern is even.

Concerning the other types of SHCs, a detailed analysis is omitted here for the sake of brevity. Instead, we just indicate the main differences with type I SHCs that affect the symmetries of the modes.

As in type I SHCs, the HODMD method (using appropriate tunable parameters) provides expansions of the form (4.7), namely

(4.22)
$$\Theta(r, \phi, t) = \sum_{n=-N_\Theta}^{N_\Theta} a_n^\Theta \Theta_n(r, \phi)\, \mathrm{e}^{\mathrm{i}\, n\, \omega_1 t}, \quad C(r, \phi, t) = \sum_{n=-N_C}^{N_C} a_n^C C_n(r, \phi)\, \mathrm{e}^{\mathrm{i}\, n\, \omega_1 t},$$

where the number of retained modes for the temperature and concentration (which do not generally coincide), $2N_\Theta + 1$ and $2N_C + 1$, respectively, depend on the considered pattern. As in type I patterns, since the left-hand sides in these expansions are real, the mean field modes, Θ_0 and C_0, are real, and the remaining oscillatory modes appear in complex conjugate pairs, namely $\Theta_n = \overline{\Theta}_{-n}$ and $C_n = \overline{C}_{-n}$, for all n, where as above the overbar denotes the complex conjugate.

- (Type III SHC) In connection with the spatial symmetries of the modes appearing in (4.22), the only difference with those of type I SHC is that instead of (4.13), the odd modes satisfy the same symmetry as the even modes, i.e.,

  (4.23)
  $$\Theta_n(r, \phi + \pi) = -\Theta_n(r, \phi), \quad C_n(r, \phi + \pi) = -C_n(r, \phi) \text{ for all } n.$$

  Thus, the temperature and concentration fields at the midplane satisfy the R_2 symmetry at every time instant. As in type I SHC solutions, in type III SHC the mid diameter along the direction of inclination is just in between two counterpropagating lanes of the SHC, which means that the number of lanes in this pattern is also even.

- (Type II SHC) The modes appearing in (4.22) exhibit a different symmetry than those appearing (4.12)–(4.13), and (4.16), namely

  (4.24)
  $$\Theta_n(r, -\phi) = \Theta_n(r, \phi), \quad C_n(r, -\phi) = C_n(r, \phi) \text{ if } n = \text{even}$$

  and

  (4.25)
  $$\Theta_n(r, -\phi) = -\Theta_n(r, \phi), \quad C_n(r, -\phi) = -C_n(r, \phi) \text{ if } n = \text{odd}.$$

  Note that, in contrast to what happened with type I SHCs, the symmetry (4.24) also holds for $n = 0$, which is considered as even, without the need of subtracting the spatial mean value of this mode. This is because the symmetry (4.24) does not require that these modes exhibit zero spatial mean value.

Consistently with (4.22), the spatio-temporal symmetry of type I SHCs (4.20) is replaced by

$$(4.26) \qquad \Theta(r, \phi, t + T/2) = \Theta(r, -\phi, t), \quad C(r, \phi, t + T/2) = C(r, -\phi, t).$$

Or, still, noting that the transformation $\phi \to -\phi$ (maintaining r) is equivalent to $(x, y) \to (x, -y)$, the spatio-temporal symmetry (4.26) can also be written as

$$(4.27) \qquad x \to x, \quad y \to -y, \quad t \to t + T/2, \quad \Theta \to \Theta, \quad C \to C.$$

Note that invariance under (4.27) now means that the mid diameter along the inclination is inside a lane of the type II SHC pattern, which in turn means that the number of lanes is odd in these patterns.

- (Type IV SHC) For these SHCs, the modes appearing in (4.22) satisfy the symmetry (4.24) but, instead of (4.25), the odd modes satisfy the same symmetry as the even modes, i.e.,

$$(4.28) \qquad \Theta_n(r, -\phi) = \Theta_n(r, \phi), \quad C_n(r, -\phi) = C_n(r, \phi) \text{ for all } n.$$

Thus, the temperature and concentration fields at the midplane satisfy the R_1 symmetry at every time instant. As in type II SHC solutions, in type IV SHC the mid diameter along the direction of inclination is inside a lane of the type IV SHC pattern, which in turn means that the number of lanes is also odd in these patterns.

4.2. Modulated SHC patterns. Now, we consider the dynamics corresponding to several modulated SHC oscillations, with amplitudes that are no longer constant (in contrast to the previous symmetric SHCs) but modulated in time. As anticipated in the introduction, these modulated patterns seem to originate in a Neimark–Sacker bifurcation [16] of the branch of periodic SHC solutions, and further bifurcations. The Neimark–Sacker bifurcation is produced by a pair of complex conjugate, nearly unstable Floquet multipliers [16] of the basic periodic SHC orbit. Thus, in principle, near the bifurcation point, an invariant two-torus is expected to exist in phase space. One of the two fundamental frequencies of the associated quasiperiodic orbit is close to the frequency of the basic periodic solution, and the other is close to that of the pair of complex nearly unstable Floquet eigenfunctions. Generically, these two fundamental frequencies are incommensurable, though they can be commensurable due to frequency locking. In fact, beyond the bifurcation point, infinitely many, quite narrow, cusped Arnold tongues [39] intersect in which frequency locking takes place. In each tongue, a pair of periodic orbits exists, one stable and the other unstable, which disappear at the border of the tongue through a saddle-node bifurcation. These periodic orbits are produced by weak resonances, and their period is generically very large. The stable periodic orbits in each tongue typically exhibit a small basin of attraction and, moreover, the transients converging to the orbits may be very slow and may somewhat wander, in a near-heteroclinic way, visiting vicinities of nearby unstable periodic orbits associated with other Arnold tongues.

With the above in mind, quasiperiodic attractors and frequency locked periodic attractors are identified by the HODMD method as follows. These attractors exhibit zero (in fact, very small but nonzero, due to numerical errors) growth/damping rates. For quasiperiodic

attractors, the relevant frequencies are linear combinations, with integer coefficients, of two or more incommensurable fundamental frequencies. When the "fundamental frequencies" become commensurable (frequency locking), the attractor is periodic and the relevant frequencies are all multiples of a fundamental frequency. It must be noted, however, that elucidating quasiperiodicity is not possible in finite precision computations, in which two frequencies are necessarily commensurable. This issue will be addressed in section 4.2.1, where a particular quasiperiodic attractor will be considered for which the associated fundamental frequencies are *nearly incommensurable*. This type of attractor can be guessed to be quasiperiodic or, at least, nearly quasiperiodic. The case of a frequency locked periodic orbit will be considered in section 4.2.2.

As anticipated in the introduction, for most values of the Rayleigh number, modulated superhighways remain irregular (namely, neither periodic nor quasiperiodic) even for extremely large time, at least, of the order of several thousand time units. These irregular orbits seem to exhibit multiple nearly heteroclinic connections, visiting vicinities of unstable periodic solutions originated in a Neimark Sacker bifurcation. The expansions (4.22) of these irregular orbits exhibit (somewhat small but) nonzero positive and negative growth rates. Positive growth rates indicate departure from an unstable periodic orbit, while negative growth rates account for the approach to another unstable periodic orbit. The irregular orbits could correspond to extremely long transients that would finally converge to attractors. However, in practice, numerical (or experimental) tests can only be performed in reasonably large timespans, meaning that ascertaining convergence to attractors is not possible in practice. Therefore, these irregular orbits will not be further pursued in this section, where the analysis will focus on periodic and quasiperiodic orbits.

4.2.1. A quasiperiodic orbit showing two incommensurable fundamental frequencies at $Ra =$ 1645.
After a long integration of the numerical solver in order to eliminate transient behavior at $Ra = 1645$, we set $t = 0$ and begin collecting snapshots to apply the HODMD method. The time evolution of the temperature and concentration at a representative point inside the spatial domain is given in Figure 4.7. Comparison with Figure 4.1 shows that while
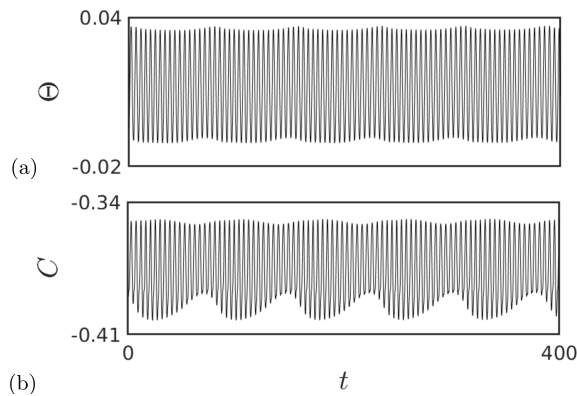

Figure 4.7. *Temporal evolution of the* (a) *temperature and* (b) *concentration at the mid-height point* $r = R/2, \phi = 45°$, *in nondimensional units, for the quasiperiodic, modulated SHC state obtained at* $Ra = 1645$.

the symmetric SHC pattern can be seen as an oscillation with constant amplitude modulation around its mean field mode, the oscillation in the present pattern exhibits a slowly varying amplitude around its mean field mode.

In order to analyze the dynamics in the present case, the HODMD method is applied to both the temperature and concentration using 801 snapshots in the time interval $0 \leq t \leq 160$, which as seen in Figure 4.1 is somewhat larger than the modulating period (namely, the larger period that is present). The HODMD method is applied using the following values of the tunable parameters:

$$(4.29) \qquad\qquad \varepsilon_1 = 10^{-5}, \quad \varepsilon_2 = 10^{-3}, \quad d = 200.$$

Comparison of (4.29) with (4.6) shows that the dimension reduction and mode truncation thresholds coincide with their counterparts in the simpler symmetric SHC pattern considered in the last subsection, which illustrates the robustness of the method. The index d, instead, is much larger now, which is consistent with the higher complexity of the present pattern. The relative RMS error, as defined in (2.24), is $2.85 \sim 10^{-3}$ retaining 45 modes for the thermal field and $\sim 2.7 \cdot 10^{-3}$ retaining 21 modes for the concentration field. Note that the selected value of the index d is fairly large, namely $d = 200$. If, instead, the value $d = 1$ were taken, which corresponds to applying the standard DMD method, then the relative RMS error would have been $\sim 3.5 \cdot 10^{-3}$ retaining 74 modes (a much larger number of modes than using $d = 200$) for the thermal field, while for the concentration field, both the relative RMS error and the number of retained modes coincide with their counterparts for $d = 200$.

For both the temperature and concentration, the damping rates identified by the method are all negative and such that $|\delta_n|$ is very small, namely smaller than $\sim 10^{-4}$. This indicates that, to the approximation relevant here, the given data are already in the attractor.

The $a - \omega$ diagrams for both the temperature and concentration are given in Figure 4.8. As can be seen, these diagrams exhibit an interesting pattern, built by seven biangular subpatterns. For both the temperature and concentration, the upper vertices (plotted in black) of the subpatterns turn out to be the zero frequency and three pairs of positive/negative harmonics of the *first fundamental frequency*

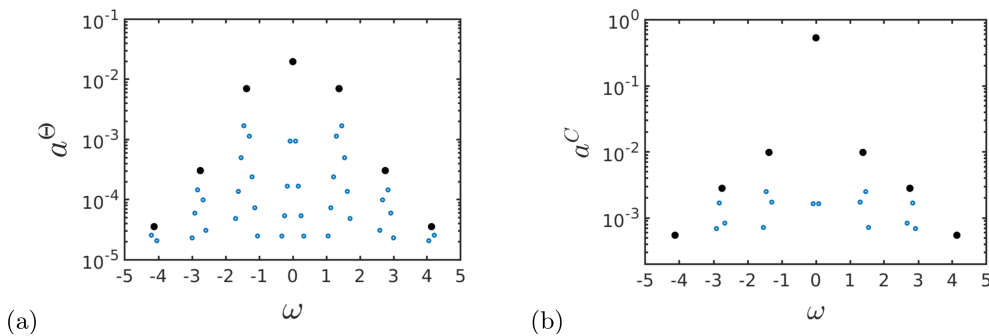
(a)   (b)

Figure 4.8. *$a - \omega$ diagrams for the temperature* (a) *and concentration* (b) *fields in the application of the HODMD method to the considered quasiperiodic, modulated SHC oscillation at* $Ra = 1645$. *Those points corresponding to the upper vertices of the seven biangular subpatterns are plotted in black, and the remaining points, in blue.*

(4.30)
$$\tilde{\omega}_1 = 1.3767,$$

which is calculated with five exact significant figures. In addition, in each subpattern, the various subsequent nearby frequencies differ from each other by a *second fundamental frequency*

(4.31)
$$\tilde{\omega}_2 = 0.0818.$$

In other words, the various frequencies identified by the method can be written, with five exact digits, as

(4.32)
$$\omega = n_1 \tilde{\omega}_1 + n_2 \tilde{\omega}_2,$$

where n_1 and n_2 are positive or negative integers. Using this, the expansions (4.1)–(4.2) can be written as

(4.33)
$$\Theta(r, \phi, t) = \sum_{n_1, n_2} a^{\Theta}_{n_1 n_2} \Theta_{n_1 n_2}(r, \phi)\, e^{i\,(n_1 \tilde{\omega}_1 + n_2 \tilde{\omega}_2)\, t},$$

(4.34)
$$C(r, \phi, t) = \sum_{n_1, n_2} a^{C}_{n_1 n_2} C_{n_1 n_2}(r, \phi)\, e^{i\,(n_1 \tilde{\omega}_1 + n_2 \tilde{\omega}_2)\, t},$$

where the relevant values of n_1 and n_2, identified by the method, are given in Table 4.1. As seen in this table, consistently with Figure 4.8(a), the method identifies 45 frequencies for the temperature, namely, the frequency $\omega = 0$ (associated with $n_1 = n_2 = 0$) and 22 pairs of positive/negative frequencies. For the concentration, consistently with Figure 4.8(b), the number of identified frequencies is 21, including the zero frequency and 10 pairs of positive/negative frequencies.

The fundamental frequencies $\tilde{\omega}_1$ and $\tilde{\omega}_2$ are nearly incommensurable, as can be seen in the analysis in the appendix. Note that, with finite precision computations, exact incommensurability is not possible, namely two double precision numbers are always commensurable. However, two frequencies, $\tilde{\omega}_1 > 0$ and $\tilde{\omega}_2 > 0$, such that $\tilde{\omega}_1 > \tilde{\omega}_2$, computed with finite precision, are nearly incommensurable if they are such that

(4.35)
$$\left| \frac{\tilde{\omega}_2}{\tilde{\omega}_1} - \frac{p}{q} \right| < \varepsilon,$$

where p and q are mutually prime, natural numbers, such that q is large and ε is conveniently small. Note that if $\tilde{\omega}_1$ and $\tilde{\omega}_2$ are approximated such that $\tilde{\omega}_2/\tilde{\omega}_1 = p/q$ (cf. (4.35)), then the resulting approximated frequencies are commensurable and the dynamics is periodic, with a fundamental frequency $\tilde{\omega} \simeq \tilde{\omega}_2/p \simeq \tilde{\omega}_1/q$, which is very small, namely its period $(2\pi/\tilde{\omega})$ is very large. Thus, the approximating periodic orbit is nearly quasiperiodic and hardly distinguishable in practice from a truly quasiperiodic solution. For the present case, as seen in the appendix (Table A.2), (4.35) holds with $p = 29$, $q = 488$, and $\varepsilon = 10^{-5}$ (comparable to the precision in the computation of the frequencies $\tilde{\omega}_1$ and $\tilde{\omega}_2$). Thus, the frequency of the abovementioned approximating periodic solution is $\tilde{\omega} \simeq \tilde{\omega}_1/q = \tilde{\omega}_2/p = 2.8 \cdot 10^{-3}$ and its period is very large, namely equal to $\simeq 2\pi/\tilde{\omega} = 2.2 \cdot 10^3$ time units. In other words, the considered orbit can be considered as quasiperiodic, or at least nearly quasiperiodic, as anticipated.

Table 4.1

The integers n_1 and n_2 appearing in the decomposition (4.32) and the associated mode amplitudes for the temperature and concentration.

ω	n_1	n_2	a^{Θ}	a^C
0	0	0	0.0197	0.532
± 0.0818	0	± 1	$9.41 \cdot 10^{-4}$	$1.64 \cdot 10^{-3}$
± 0.1636	0	± 2	$1.68 \cdot 10^{-4}$	$-$
± 0.2454	0	± 3	$5.4 \cdot 10^{-5}$	$-$
± 0.327	0	± 4	$2.48 \cdot 10^{-5}$	$-$
± 1.05	± 1	∓ 4	$2.5 \cdot 10^{-5}$	$-$
± 1.131	± 1	∓ 3	$7.33 \cdot 10^{-5}$	$-$
± 1.213	± 1	∓ 2	$2.39 \cdot 10^{-4}$	$-$
± 1.295	± 1	∓ 1	$1.14 \cdot 10^{-3}$	$1.74 \cdot 10^{-3}$
± 1.377	± 1	0	$7.02 \cdot 10^{-3}$	$9.83 \cdot 10^{-3}$
± 1.459	± 1	± 1	$1.69 \cdot 10^{-3}$	$2.51 \cdot 10^{-3}$
± 1.54	± 1	± 2	$4.98 \cdot 10^{-4}$	$7.18 \cdot 10^{-4}$
± 1.622	± 1	± 3	$1.37 \cdot 10^{-4}$	$-$
± 1.704	± 1	± 4	$4.87 \cdot 10^{-5}$	$-$
± 2.59	± 2	∓ 2	$3.09 \cdot 10^{-5}$	$-$
± 2.672	± 2	∓ 1	$9.92 \cdot 10^{-5}$	$8.37 \cdot 10^{-4}$
± 2.753	± 2	0	$3.05 \cdot 10^{-4}$	$2.82 \cdot 10^{-4}$
± 2.835	± 2	± 1	$1.46 \cdot 10^{-4}$	$1.69 \cdot 10^{-3}$
± 2.917	± 2	± 2	$5.99 \cdot 10^{-5}$	$6.92 \cdot 10^{-4}$
± 2.999	± 2	± 3	$2.32 \cdot 10^{-5}$	$-$
± 4.048	± 3	∓ 1	$2.08 \cdot 10^{-5}$	$-$
± 4.13	± 3	0	$3.57 \cdot 10^{-5}$	$5.49 \cdot 10^{-4}$
± 4.212	± 3	± 1	$2.57 \cdot 10^{-5}$	$-$

Let us now analyze the symmetries of the modes appearing in the expansion (4.33)–(4.34), which are now seen to be consistent with the symmetries of the modes of the type I symmetric SHCs considered in section 4.1. This suggests that the present quasiperiodic solution bifurcates (through a Neimark–Sacker instability, as anticipated) from the type I symmetric SHC branch.

The counterpart of the symmetries (4.12) and (4.13) are now given by

$$\Theta_{n_1 n_2}(r, \phi + \pi) = -\Theta_{n_1 n_2}(r, \phi), \quad C_{n_1 n_2}(r, \phi + \pi) = -C_{n_1 n_2}(r, \phi)$$
$$\text{(4.36)} \qquad \qquad \qquad \text{if } n_1 = \text{even with } (n_1, n_2) \neq (0, 0),$$

and

$$\text{(4.37)} \qquad \Theta_{n_1 n_2}(r, \phi + \pi) = \Theta_{n_1 n_2}(r, \phi), \quad C_{n_1 n_2}(r, \phi + \pi) = C_{n_1 n_2}(r, \phi) \text{ if } n_1 = \text{odd},$$

respectively (see Figure 4.9). Note that, as indicated, the symmetry (4.36) is satisfied for $n_1 = 0$ and all values of n_2. This means that the modes associated to frequency ω_2 only ($n_1 = 0$) are R_2 symmetric, as can be appreciated in Figure 4.9(a). As a result, the symmetry of the remaining modes ($n_1 \neq 0$) is determined only by the value of n_1 and is the same as in type I SHC solutions.

However, as in symmetric type I SHCs, this symmetry (4.36) does not apply to C_{00}, while it applies to Θ_{00} only approximately. This is because, by its own nature, this symmetry
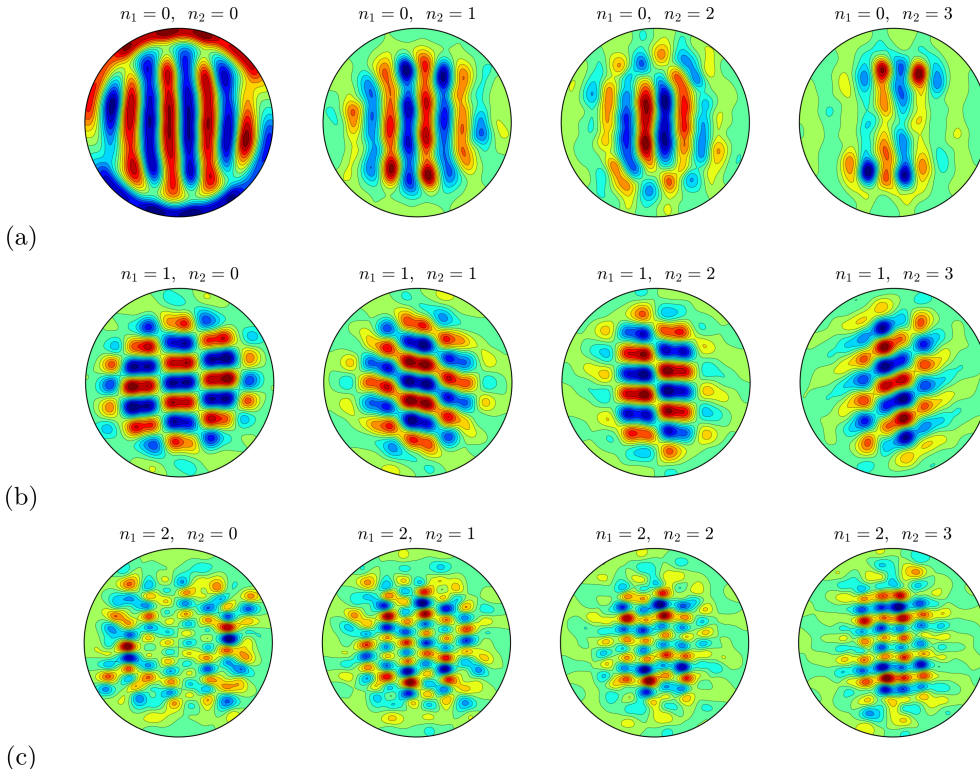
Figure 4.9. *Quasiperiodic orbit obtained for $Ra = 1645$: contours of the real part of the temperature modes associated to the values of the indexes n_1 and n_2 in expansion (4.33) indicated in the figure. The depicted modes correspond to (a) $n_1 = 0$, (b) $n_1 = 1$, and (c) $n_1 = 2$, and four different values of n_2.*

requires that the mode exhibits zero spatial mean value. The spatial mean values of Θ_{00} and C_{00} are not zero, but they turn out to be

$$(4.38) \qquad \Theta_{00}^{\text{mean}} = 3.2 \cdot 10^{-4}, \quad C_{00}^{\text{mean}} = -0.94.$$

Thus, $\Theta_{00}^{\text{mean}}$ is very small, but C_{00}^{mean} is not, which explains that (4.36) approximately applies to Θ_{00} but not to C_{00}. If we multiple $\Theta_{00}^{\text{mean}}$ by a_{00}^{Θ} we obtain $\Theta^{\text{STmean}} \simeq 6.29 \cdot 10^{-6}$, which is a very small value compared with the actual values of Θ in the mid-height plane. As we discuss below, this is a consequence of the fact that the two-torus is R_2-symmetric.

As in type I symmetric SHCs, we define the *spatio-temporal mean field mode*, C_{00}^{STMFM}, by substracting C_{00}^{mean} from the temporal mean field mode, C_{00}. This gives the counterpart of (4.15), namely

$$(4.39) \qquad C_{00}^{\text{STMFM}} = C_{00} - C_{00}^{\text{mean}}.$$

To the approximation relevant here, these modes do satisfy the symmetry (4.36), namely

$$(4.40) \qquad \Theta_{00}(r, \phi + \pi) = -\Theta_{00}(r, \phi), \quad C_{00}^{\text{STMFM}}(r, \phi + \pi) = -C_{00}^{\text{STMFM}}(r, \phi).$$

To proceed, we multiply C_{00}^{mean} by a_{00}^{C}. This gives the *spatio-temporal mean* of the concentration, C^{STmean}, along the quasiperiodic attractor, namely

(4.41)
$$C^{\mathrm{STmean}} \equiv a_{00}^c \, C_0^{\mathrm{mean}} \simeq -0.5.$$

Using (4.39)–(4.41), the expansions (4.33) and (4.34) can be rewritten as

(4.42)
$$\Theta(r, \phi, t) = a_{00}^\Theta \, \Theta_{00}(r, \phi) + \sum_{(n_1, n_2) \neq (0,0)} a_{n_1 n_2}^\Theta \, \Theta_{n_1 n_2}(r, \phi) \, \mathrm{e}^{\mathrm{i}\,(n_1 \tilde{\omega}_1 + n_2 \tilde{\omega}_2)\, t}$$

and

(4.43)
$$\begin{aligned} C(r, \phi) = C^{\mathrm{STmean}} + a_{00}^C \, C_{00}^{\mathrm{STMFM}}(r, \phi) + \\ \sum_{(n_1, n_2) \neq (0,0)} a_{n_1 n_2}^C \, C_{n_1 n_2}(r, \phi) \, \mathrm{e}^{\mathrm{i}\,(n_1 \tilde{\omega}_1 + n_2 \tilde{\omega}_2)\, t}, \end{aligned}$$

respectively.

In contrast to the analysis of symmetric type I SHCs presented in section 4.1, identifying spatio-temporal symmetries in the present quasiperiodic attractor is a subtle matter. Instead, a reflection symmetry will be identified in the associated two-torus filled by the orbit. A semianalytic, parametric approximation of this torus is readily obtained from (4.42)–(4.43), to be

(4.44)
$$\begin{aligned} \Theta(r, \phi, \phi_1, \phi_2) = a_{00}^\Theta \Theta_{00}(r, \phi) \\ + \sum_{(n_1, n_2) \neq (0,0)} a_{n_1 n_2}^\Theta \Theta_{n_1 n_2}(r, \phi) \, \mathrm{e}^{\mathrm{i}\,(n_1 \phi_1 + n_2 \phi_2)} \quad \text{for } 0 \leq \phi_1, \phi_2 < \pi, \end{aligned}$$

(4.45)
$$\begin{aligned} C(r, \phi, \phi_1, \phi_2) = C^{\mathrm{STmean}} + a_{00}^C C_{00}^{\mathrm{STMFM}}(r, \phi) \\ + \sum_{(n_1, n_2) \neq (0,0)} a_{n_1 n_2}^C C_{n_1 n_2}(r, \phi) \, \mathrm{e}^{\mathrm{i}\,(n_1 \phi_1 + n_2 \phi_2)} \quad \text{for } 0 \leq \phi_1, \phi_2 < \pi, \end{aligned}$$

where ϕ_1 and ϕ_2 are two parameters along the two-torus in phase space.

Now, noting that $\mathrm{e}^{\mathrm{i}\,n_1 \pi} = 1$ and -1 for $n_1 = $ even and odd, respectively, (4.36)–(4.37) and (4.39)–(4.41) imply that, to the approximation relevant here, the parametric representation of the two-torus (4.44)–(4.45) exhibits the following spatio-temporal reflection symmetry:

(4.46)
$$\Theta(r, \phi, \phi_1 + \pi, \phi_2) = -\Theta(r, \phi + \pi, \phi_1, \phi_2),$$

(4.47)
$$C(r, \phi, \phi_1 + \pi, \phi_2) - C^{\mathrm{STmean}} = -\left[C(r, \phi + \pi, \phi_1, \phi_2) - C^{\mathrm{STmean}} \right].$$

Since the transformation $\phi \to \phi + \pi$ (maintaining r) is equivalent to $(x, y) \to -(x, y)$, the spatio-temporal symmetry (4.46)–(4.47) can also be written as

(4.48)
$$\begin{aligned} x \to -x, \quad y \to -y, \quad \phi_1 \to \phi_1 + \pi, \\ \Theta \to -\Theta, \quad C - C^{\mathrm{STmean}} \to -\left(C - C^{\mathrm{STmean}} \right). \end{aligned}$$

In other words, to the approximation relevant here, the two-torus is reflection symmetric in phase space around the origin $(x, y) = (0, 0)$. This reflection symmetry is illustrated in Figure 4.10, where the time evolution of the value of concentration minus its *spatio-temporal*
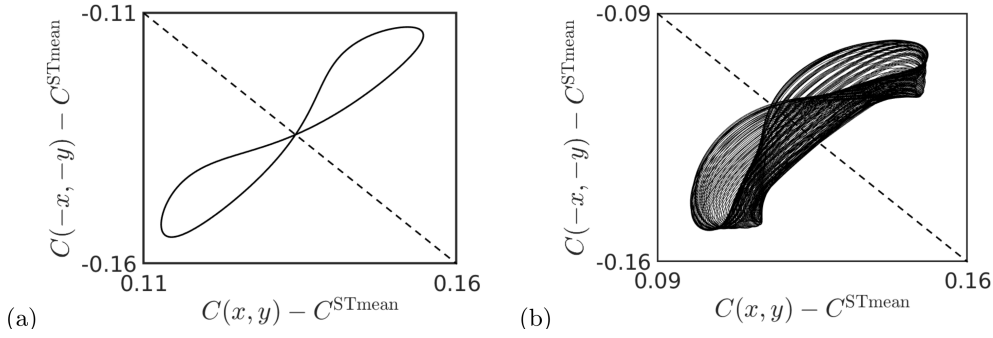
Figure 4.10. *Phase portrait of the value of concentration minus its spatio-temporal mean C^{STmean} in two symmetric points, (x, y) and $(-x, -y)$ for* (a) *the symmetric SHC obtained for $Ra = 1610$ and* (b) *the two-torus obtained for $Ra = 1645$.*

mean C^{STmean} in two symmetric points, (x, y) and $(-x, -y)$, is represented, both for the symmetric SHC obtained for $Ra = 1610$, in plot (a), and for the present two-torus obtained for $Ra = 1645$, in plot (b). As can be seen, both plots exhibit the symmetry (4.48), as anticipated. Also, while for the periodic attractor at $Ra = 1610$ the orbit is contained in a closed curve, for the quasiperiodic attractor at $Ra = 1645$, the orbit fills a 2D region in the considered plane.

4.2.2. A frequency locked periodic orbit at $Ra = $1680. For this value of Ra, the dynamics is associated with a periodic attractor that corresponds to a frequency locked orbit.

In order to ensure that the considered data are already in the attractor, we first integrate the numerical solver in a very large time interval to eliminate transient behavior. After this, we set $t = 0$ and begin collecting snapshots to apply the HODMD method.

The temporal evolution of the temperature and concentration at a representative point inside the spatial domain is considered in Figure 4.11. As can be seen in this figure, as time proceeds, the pattern alternates between modulated SHC structures (near, e.g., $t = 101$) and nearly stationary longitudinal rolls (near, e.g., $t = 150$). Notice that these latter rolls are not aligned along inclination and, also, that the number of lanes is odd. These are in contrast to the previously analyzed symmetric SHC obtained for $Ra = 1610$ and in contrast to the quasi-periodic orbit obtained for $Ra = 1645$.

In order to analyze the dynamics in the present case, the HODMD method is applied to both the temperature and concentration using 701 snapshots in the time interval $0 \leq t \leq 140$, with the following values of the remaining tunable parameters:

$$(4.49) \qquad\qquad \varepsilon_1 = 5 \cdot 10^{-5}, \quad \varepsilon_2 = 5 \cdot 10^{-4}, \quad d = 200.$$

Comparison with their counterparts in (4.29) for the quasiperiodic attractor shows that these parameters are similar in the present case to obtain comparable accuracy of the reconstructions. In fact, the relative RMS error, as defined in (2.24), is $\sim 1.32 \cdot 10^{-3}$ retaining 149 modes for the thermal field and $\sim 3.2 \cdot 10^{-3}$ retaining 99 modes for the concentration field. As for the quasiperiodic attractor, the selected value of the index d is fairly large, namely $d = 200$. If, instead, the value $d = 1$ were taken, which corresponds to applying the standard DMD
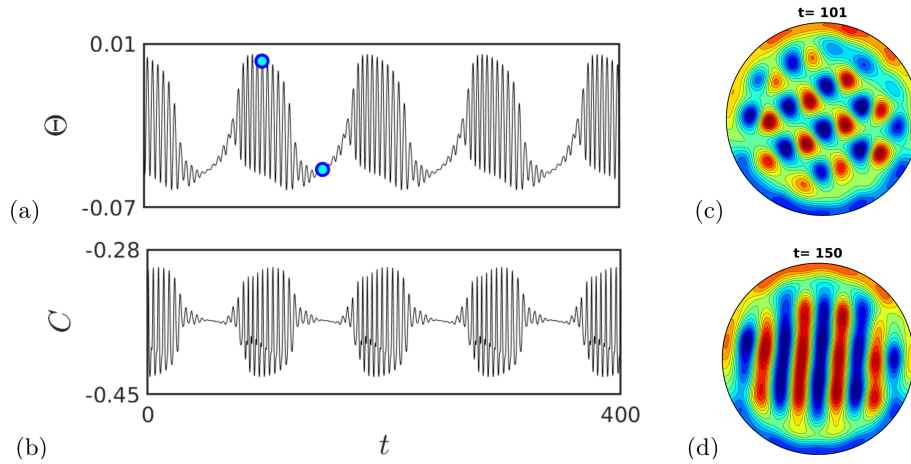
(a)

(b)

(c)

(d)

Figure 4.11. *Time series of* (a) *temperature and* (b) *concentration at a representative interior point in the spatial domain for the periodic, modulated SHC state obtained at Ra = 1680. Contour plots of temperature at midplane for the time instants* (c) $t = 101$ *and* (d) $t = 150$, *indicated in the temperature time series with a circle.*
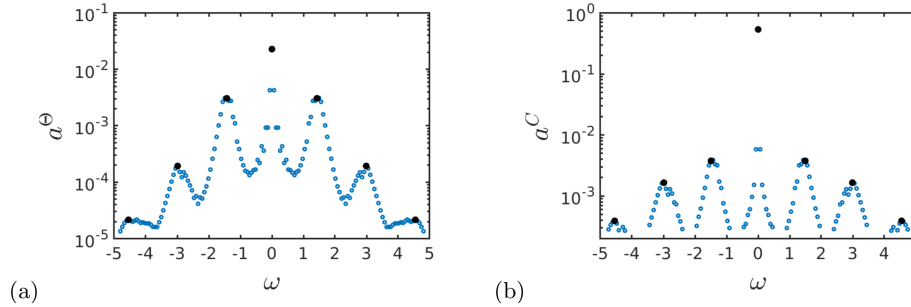

(a)

(b)

Figure 4.12. $a - \omega$ *diagrams for the temperature* (a) *and the concentration* (b) *fields in the application of the HODMD method to the periodic, modulated SHC state. Those points corresponding to the upper vertices of the seven biangular subpatterns are plotted in black, and the remaining points, in blue.*

method, then the relative RMS error would have been much larger, namely ~ 0.045 for the thermal field and ~ 0.01 for the concentration field.

The damping rates identified by the method are all negative and such that $|\delta_n|$ is very small, namely $|\delta_n|$ is smaller than $\sim 10^{-6}$ for both the temperature and concentration. This indicates that, to the approximation relevant here, the given data are already in the attractor.

The $a - \omega$ diagrams for both the temperature and concentration are given in Figure 4.12. As can be seen, these diagrams are qualitatively similar to their counterparts for the quasi-periodic dynamics analyzed in section 4.2.1 (cf. Figure 4.8). In other words, for both the concentration and temperature, the relevant points in the $a - \omega$ diagrams build seven biangular subpatterns, whose upper vertices are the zero frequency (associated with the mean field) and three positive and negative harmonics of the *primary fundamental frequency,*

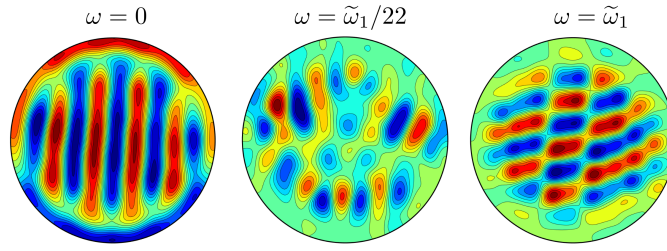$$(4.50) \qquad\qquad\qquad \tilde{\omega}_1 = 1.4287.$$

Figure 4.13. *Frequency locked periodic orbit obtained for Ra = 1680: contours of the real part of the temperature modes associated to frequencies $\omega = 0$, $\omega = \widetilde{\omega}_2 = \widetilde{\omega}_1/22$, and $\omega = \widetilde{\omega}_1$.*

In all biangular subpatterns, all nearby frequencies differ among each other by the *secondary fundamental frequency*

$$(4.51) \qquad\qquad \widetilde{\omega}_2 = 0.064939.$$

In principle, one could think that the pattern is quasiperiodic, as it happened in section 4.2.1. However, in the present case, $\tilde{\omega}_1$ and $\tilde{\omega}_2$ are commensurable (which is consistent with frequency locking), namely $\widetilde{\omega}_1 = 22\,\widetilde{\omega}_2$, with an accuracy of five significant digits. Thus, in the present case, to the approximation relevant here, the pattern is periodic, with a period $T = 2\pi/\widetilde{\omega}_2 = 96.755$ time units.

Quantitative inspection of the modes retained in the present case shows that, in contrast to what happened in the symmetric and modulated dynamics analyzed in sections 4.1 and 4.2.1, none of the modes identified by the HODMD method shows any identifiable symmetry, as can be appreciated in Figure 4.13, where the real part of the temperature modes associated to frequencies $\omega = 0$, $\omega = \widetilde{\omega}_2 = \widetilde{\omega}_1/22$, and $\omega = \widetilde{\omega}_1$ are displayed. Note that the possible symmetries would result from the symmetries of the problem. Concentrating on the symmetries of the temperature and concentration at the midplane of the cylinder, these symmetries of the modes consist on invariance under any of the actions

$$(4.52) \qquad\qquad R_1^{\pm}: \quad y \to -y, \quad \Theta \to \pm\Theta, \quad C \to \pm C,$$

$$(4.53) \qquad\qquad R_2^{\pm}: \quad x \to -x, \quad y \to -y, \quad \Theta \to \mp\Theta, \quad C \to \mp C.$$

Since the modes are not invariant under any of these actions, the dynamics of the present pattern does not exhibit any of the possible spatio-temporal symmetries.

5. Concluding remarks. We have concentrated on the relevant patterns appearing in double-diffusive convection in a fairly flat, slightly inclined circular cylinder. These patterns were analyzed using a recent data processing tool called higher order dynamic mode decomposition (HODMD), which was applied to numerically obtained data. Specifically, we have considered symmetric periodic and modulated superhighway (SHC) patterns. The advantage of using HODMD is that it allows us to discard transient dynamics and facilitates identifying the temporal nature of the solutions, avoiding the use of FFTs and Poincaré sections, which require extremely long and precise time integrations.

For symmetric SHC patterns, considered in section 4.1, the HODMD method permitted uncovering the global spatio-temporal structure of these patterns as a superposition of a mean

field and a periodic oscillation. The qualitative spatio-temporal structure of the thermal SHC patterns was proved to be well described using just the mean field mode and the dominant oscillatory mode. The mean field for the temperature turned out to be longitudinal rolls aligned with inclination, each roll coincident with the lanes in the SHC pattern. The first oscillatory mode were transverse oscillations in which elongated convective cells split and merge in a pendular motion. The amplitudes of these two first modes are of the same order, and much larger than those associated to the following oscillatory harmonics. In the reconstruction of the solution with the modes provided by HODMD, the hotter/colder lanes in the longitudinal rolls are either reinforced or canceled out when the lanes with alternating hotter/colder spots of the first oscillatory mode are superposed to the mean flow, resulting in the peculiar SHC spatio-temporal structure. In contrast, the spatio-temporal structure of the concentration SHC patterns also required us to consider the second and subsequent oscillatory harmonics. The spatial complexity of the concentration field arises, on one hand, from the smaller spatial wavelenghts of these oscillatory harmonics and, on the other, from the fact that the concentration mean field is very spatially irregular.

With the reconstruction of the solution with the modes provided by HODMD we are able to assert that the periodic SHC states originate from a Hopf instability of the basic steady pattern of longitudinal rolls. We have focused on type I symmetric periodic SHC patterns and have analyzed the symmetries of the modes of the HODMD decomposition. We have also discussed the spatial symmetries that the oscillatory modes of the rest of symmetric periodic SHC solutions would exhibit when the HODMD method is applied using information at midplane. HODMD allows us either to identify or discard the spatio-temporal symmetries that the 3D patterns would exhibit. Using solutions at midplane is particulary useful to extract information about type I and type III symmetric solutions, which involve the R_2^{3D} symmetry. Otherwise, two equidistant planes should be used and the modes and coefficients of the HDOMD expansions should be related in both planes.

Concerning the modulated SHC patterns analyzed in section 4.2, these exhibit a spatial modulation that gives a slowly varying amplitude (in contrast to symmetric SHCs, which exhibit a constant amplitude). Two representative modulated SHCs were considered. Quasiperiodic modulated SHCs were addressed in section 4.2.1, where quasiperiodicity was guessed using a method described in the appendix. Again, the HODMD method facilitated the identification of the symmetries that are present. In this case, the symmetry manifests itself in a reflection symmetry exhibited by the two-torus filled by the orbit. A semianalytic description of the torus was derived as a part of the analysis. In addition, a frequency locked periodic orbit was considered in section 4.2.2. In this case, the HODMD method permitted to ensure that the pattern is periodic, namely all frequencies were seen (with great precision) to be multiples of a unique fundamental frequency. It must be noted that, in this case, strict periodicity cannot be guessed from a look at the obtained time series, which would resemble their counterparts obtained in a quasiperiodic case.

We hope that the present paper illustrates the ability of the HODMD method to uncover the structure of complex pattern forming phenomena.

Appendix A. Nearly incommensurable frequencies. This is a subtle matter for finite precision frequencies, which are always commensurable. However, two frequencies computed

with finite precision, ω_1 and ω_2, are guessed to be incommensurable if they are nearly incommensurable, which means that they are such that

$$(A.1) \qquad \left| \frac{\omega_2}{\omega_1} - \frac{p}{q} \right| < \varepsilon,$$

where the fraction p/q is *irreducible*, namely the natural numbers and $q > p > 0$ are mutually prime, q is large (say, larger than 100), and $\varepsilon > 0$ is conveniently small.

Approximations of ω_2/ω_1 by irreducible fractions are obtained using an iterative method based on Haros–Farey fractions [40], which is based on the property that if $r_0 = p_0/q_0$ and $r_1 = p_1/q_1$ are two irreducible fractions such that $0 < r_0 < r_1 < 1$, then the *mediant* of these two fractions, defined as

$$(A.2) \qquad \widehat{r} = \frac{p_0 + p_1}{q_0 + q_1},$$

is also irreducible and such that $r_0 < \widehat{r} < r_1$.

Without loss of generality, we assume that the frequencies ω_1 and ω_2 are such that $0 < r = \omega_2/\omega_1 < 1$. Note that for $r = 0$ and 1, ω_1 and ω_2 are commensurable, and that if $r > 1$, then interchanging ω_1 and ω_2, the new value of r is smaller than 1.

Rational approximations of r by irreducible fractions are computed iteratively as follows. Let p_0^{low}, q_0^{low}, p_0^{up}, and q_0^{up} be such that $r_0^{\mathrm{low}} = p_0^{\mathrm{low}}/q_0^{\mathrm{low}}$ and $r_0^{\mathrm{up}} = p_0^{\mathrm{up}}/q_0^{\mathrm{up}}$ are both irreducible and verify $r_0^{\mathrm{low}} < r < r_0^{\mathrm{up}}$. In the absence of a better initial guess, a selection of these irreducible initial fractions is

$$(A.3) \qquad p_0^{\mathrm{low}} = 0, \quad q_0^{\mathrm{low}} = p_0^{\mathrm{up}} = q_0^{\mathrm{up}} = 1.$$

For $n \geq 1$, we consider the mediant of the irreducible fractions $r_{n-1}^{\mathrm{low}} = p_{n-1}^{\mathrm{low}}/q_{n-1}^{\mathrm{low}}$ and $r_{n-1}^{\mathrm{up}} = p_{n-1}^{\mathrm{up}}/q_{n-1}^{\mathrm{up}}$, denoted as

$$(A.4) \qquad \widehat{r}_n = \frac{\widehat{p}_n}{\widehat{q}_n}.$$

As anticipated, the mediant is also irreducible and such that

$$(A.5) \qquad r_{n-1}^{\mathrm{low}} < \widehat{r}_n < r_{n-1}^{\mathrm{up}}.$$

Now, we consider two alternatives, depending on the relative position of $\widehat{r}_n$ and r:

- If $\widehat{r}_n \leq r$, then we define the next pair of irreducible fractions for the next iteration as

$$(A.6) \qquad p_n^{\mathrm{low}} = \widehat{p}_n, \quad q_n^{\mathrm{low}} = \widehat{q}_n, \quad p_n^{\mathrm{up}} = p_{n-1}^{\mathrm{up}}, \quad \text{and} \quad q_n^{\mathrm{up}} = q_{n-1}^{\mathrm{up}}.$$

- If $\widehat{r}_n > r$, then we set

$$(A.7) \qquad p_n^{\mathrm{low}} = p_{n-1}^{\mathrm{low}}, \quad q_n^{\mathrm{low}} = q_{n-1}^{\mathrm{low}}, \quad p_n^{\mathrm{up}} = \widehat{p}_n, \quad \text{and} \quad q_n^{\mathrm{up}} = \widehat{q}_n.$$

Table A.1

Irreducible fractions p/q approximating the ratio ω_2/ω_1 and the associated errors for the incommensurable frequencies $\omega_1 = \pi$ and $\omega_2 = \sqrt{2}$.

Iterations	p	q	$\lvert\omega_2/\omega_1 - p/q\rvert$
1-3	1	2	0.05
4	3	7	0.022
5	4	9	$7.7 \cdot 10^{-3}$
6	5	11	$4.4 \cdot 10^{-3}$
7-14	9	20	$1.6 \cdot 10^{-4}$
15	77	171	$1.3 \cdot 10^{-4}$
16	86	191	10^{-4}
17	95	211	$7.9 \cdot 10^{-5}$
18	104	231	$5.8 \cdot 10^{-5}$
19	113	251	$4.1 \cdot 10^{-5}$
20	122	271	$2.6 \cdot 10^{-5}$
21	131	291	$1.4 \cdot 10^{-5}$
22-23	140	311	$2.6 \cdot 10^{-6}$
24	289	642	$2.4 \cdot 10^{-6}$
25	429	953	$7.6 \cdot 10^{-7}$
26-29	569	1264	$7 \cdot 10^{-8}$
30	2705	6009	$6.2 \cdot 10^{-8}$
31	3274	7273	$6.2 \cdot 10^{-8}$
32	3843	8537	$2.3 \cdot 10^{-8}$
33	4412	9801	$1.1 \cdot 10^{-8}$
34-36	4981	11065	$1.7 \cdot 10^{-9}$
37	15512	34459	$8.9 \cdot 10^{-10}$
38	20493	45524	$2.5 \cdot 10^{-10}$
39	25474	56589	$1.3 \cdot 10^{-10}$
40	45967	102113	$4 \cdot 10^{-11}$
41	71441	158702	$2.1 \cdot 10^{-11}$
42-43	117408	260815	$2.8 \cdot 10^{-12}$
44	306257	680332	$2.8 \cdot 10^{-12}$
45	423665	941147	$1.2 \cdot 10^{-12}$
46	541073	1201962	$3.4 \cdot 10^{-13}$
47	658481	1462777	$2.2 \cdot 10^{-3}$
48-49	1199554	2664739	$3.2 \cdot 10^{-14}$
50	3057589	6792255	$2.3 \cdot 10^{-14}$
51	4257143	9456994	$7.6 \cdot 10^{-15}$
52-54	5456697	12121733	$1.1 \cdot 10^{-15}$
55	20627234	45822193	$6.7 \cdot 10^{-16}$

We define the irreducible fractions

$$\text{(A.8)} \qquad r_n^{\mathrm{low}} = \frac{p_n^{\mathrm{low}}}{q_n^{\mathrm{low}}} \quad \text{and} \quad r_n^{\mathrm{up}} = \frac{p_n^{\mathrm{up}}}{q_n^{\mathrm{up}}}.$$

Note that the length of the interval $[r_n^{\mathrm{low}}, r_n^{\mathrm{low}}]$ strictly decreases as n increases, and this interval contains r in its interior. This means that the end-points of the interval both converge to r. At this iteration, we select as approximation of r that end-point of the interval that is closest to r. This end-point will be denoted as r_n^* and the iteration is terminated when

$$\text{(A.9)} \qquad \lvert r_n^* - r\rvert < \varepsilon$$

Table A.2
Counterpart of Table A.1 for $\omega_1 = 1.3767$ and $\omega_2 = 0.0818$.

Iterations	p	q	$|\omega_2/\omega_1 - p/q|$
1-7	0	1	0.059
8	1	9	0.052
9	1	10	0.04
10	1	11	0.031
11	1	12	0.024
12	1	13	0.018
13	1	14	0.012
14	1	15	$7.2 \cdot 10^{-3}$
15	1	16	$3.1 \cdot 10^{-3}$
16-17	1	17	$5.9 \cdot 10^{-4}$
18	3	50	$5.8 \cdot 10^{-4}$
19	4	67	$2.8 \cdot 10^{-4}$
20	5	84	$1.1 \cdot 10^{-4}$
21-24	6	101	$1.2 \cdot 10^{-5}$
25	29	488	$8.8 \cdot 10^{-6}$
26	35	589	$5.3 \cdot 10^{-6}$
27	41	690	$2.8 \cdot 10^{-6}$
28	47	791	10^{-6}
29	53	892	$4.1 \cdot 10^{-7}$
30	100	1683	$2.6 \cdot 10^{-7}$
31-33	153	2575	$2.8 \cdot 10^{-8}$
34	512	8617	$1.7 \cdot 10^{-8}$
35	665	11192	$6.4 \cdot 10^{-9}$
36	818	13767	$6.9 \cdot 10^{-18}$

for some conveniently small threshold ε. It must be noted that it may happen that one of the end-points of the interval, namely either r_n^{low} or r_n^{up}, remains constant along various iterations. This means that the end-point giving the best approximation of r, namely r_n^*, may also remain constant along some iterations.

The method described above is easily implemented in a MATLAB function whose operation is very fast. Let us now illustrate the method considering two cases.

For $\omega_1 = \pi$ and $\omega_2 = \sqrt{2}$, the 55 iterations needed to obtain the approximation (A.1), with zero-machine accuracy, are given in Table A.1. Note that, as anticipated, the approximating irreducible fraction, p/q, remains constant along some of the iterations. As can be seen, setting $\varepsilon = 10^{-5}$, the method gives the approximation in 22 iterations, with $p = 140$, $q = 311$, within an accuracy $\sim 2.6 \cdot 10^{-6}$.

As a second application, we take $\omega_1 = 1.3767$, $\omega_2 = 0.0818$, which according to (4.30) and (4.31) is precisely the case needed for the dynamics considered in section 4.2.1. Now, the method needs 36 iterations to get zero-machine accuracy, as shown in Table A.2. As in the former case, the approximating irreducible fraction, p/q, remains constant along some of the iterations. Note that now, setting $\varepsilon = 10^{-5}$ as in the former case, the method gives the approximation in 25 iterations, with $p = 29$, $q = 488$, within an accuracy $\sim 8.8 \cdot 10^{-6}$.

method presented in the appendix. In particular, a FORTRAN routine implementing the method was provided by them several years ago to the last author of this paper. Also, we thank two anonymous referees for several useful comments that helped to improve the presentation of the results.

REFERENCES

[1] M. Lappa, *Thermal Convection: Patterns, Evolution and Stability*, John Wiley and Sons, New York, 2010.

[2] M. C. Cross and P. C. Hohenberg, *Pattern formation outside of equilibrium*, Rev. Mod. Phys., 65 (1993), pp. 851–1112.

[3] M. Lücke, W. Barten, P. Büchel, C. Fütterer, St. Hollinger, and Ch. Jung, *Pattern formation in binary fluid convection and in systems with throughflow*, in Evolution of Spontaneous Structures in Dissipative Continous Systems, Lecture Notes in Phys. 55, F. H. Busse and S. C. Müller, eds., Springer-Verlag, Berlin, 1998, p. 127.

[4] A. Alonso, O. Batiste, A. Meseguer, and I. Mercader, *Complex dynamical states in binary mixture convection with weak negative Soret coupling*, Phys. Rev. E, 75 (2007), 026310.

[5] P. Le Gal, A. Pocheau, and V. Croquette, *Square versus roll pattern at convective threshold*, Phys. Rev. Lett., 54 (1985), pp. 2501–2504.

[6] E. Moses and V. Steinberg, *Competing patterns in a convective binary mixture*, Phys. Rev. Lett., 57 (1986), pp. 2018–2021.

[7] E. Bodenschatz, W. Pesch, and G. Ahlers, *Recent developements in Rayleigh-Bénard convection*, Annu. Rev. Fluid Mech., 32 (2000), pp. 709–778.

[8] K. E. Daniels, B. B. Plapp, and E. Bodenschatz, *Pattern formation in inclined layer convection*, Phys. Rev. Lett., 84 (2000), pp. 5320–5323.

[9] K. E. Daniels, O. Brausch, W. Pesch, and E. Bodenschatz, *Competition and bistability of ordered undulations and undulation chaos in inclined layer convection*, J. Fluid Mech., 597 (2008), pp. 261–282.

[10] P. Subramanian, O. Brausch, K. E. Daniels, E. Bodenschatz, T. M. Schneider, and W. Pesch, *Spatio-temporal patterns in inclined layer convection*, J. Fluid Mech., 794 (2016), pp. 719–745.

[11] F. Reetz and T.M. Schneider, *Invariant states in inclined layer convection. Part 1. Temporal transitions along dynamical connections between invariant states*, J. Fluid Mech., 898 (2020), A22.

[12] F. Reetz, P. Subramanian, and T.M. Schneider, *Invariant states in inclined layer convection. Part 2. Bifurcations and connections between branches of invariant states*, J. Fluid Mech., 898 (2020), A23.

[13] F. Croccolo, F. Scheffold, and A. Vailati, *Effect of marginal inclination on pattern formation in a binary liquid mixture under thermal stress*, Phys. Rev. Lett., 111 (2013), 014502.

[14] A. Alonso, I. Mercader, and O. Batiste, *Time-dependent patterns in quasivertical cylindrical binary convection*, Phys. Rev. E, 97 (2018), 023108.

[15] S. Castellini, M. Carpineti, F. Croccolo, and A. Vailati, *Inclined convection in a layer of liquid water with poorly conducting boundaries*, Phys. Rev. Res., 2 (2020), 033481.

[16] Yu. A. Kuznetsov, *Elements of Applied Bifurcation Theory*, Springer-Verlag, Berlin, 2004.

[17] S. Le Clainche and J.M. Vega, *Higher order dynamic mode decomposition*, SIAM J. Appl. Dyn. Syst., 16 (2017), pp. 882–925.

[18] P. J. Schmid and J. L. Sesterhenn, *Dynamic mode decomposition of numerical and experimental data*, in 61st APS meeting, San Antonio, 2008, p. 208.

[19] C. W. Rowley, I. Mezić, S. Bagheri, P. Schlatter, and D. S. Henningson, *Spectral analysis of nonlinear flows*, J. Fluid Mech., 641 (2009), pp. 115–127.

[20] P. J. Schmid, *Dynamic mode decomposition of numerical and experimental data*, J. Fluid Mech., 656 (2010), pp. 5–28.

[21] J. H. Tu, C. Rowley, D. M. Luchtemburg, S. L. Brunton, and J. N. Kutz, *On dynamic mode decomposition: Theory and applications*, J. Comput. Dyn., 1 (2014), pp. 391–421.

[22] T. Sauer, J. A. York, and M. Casdagli, *Embedology*, J. Stat. Phys., 65 (1991), pp. 579–616.

[23] F. Takens, *Detecting strange attractors in turbulence*, in Dynamical Systems and Turbulence, Lecture Notes in Math. 898, D. A. Rand and L.-S. Young., eds., Springer, Berlin, 1981, pp. 366–381.

[24] J. M. Vega and S. Le Clainche, *Higher Order Dynamic Mode Decomposition and Its Applications*, Academic Press, New York, 2020.

[25] S. Le Clainche and J. M. Vega, *Spatio-temporal Koopman decomposition*, J. Nonlinear Sci., 28 (2018), pp. 1793–1842.

[26] J. Sánchez, M. Net, and J. M. Vega, *Analyzing thermal convection in a two-dimensional circular annulus via spatio-temporal Koopman decomposition*, Phys. D, 402 (2020), 132257.

[27] S. Le Clainche and J. M. Vega, *Higher order dynamic mode decomposition to identify and extrapolate flow patterns*, Phys. Fluids, 29 (2017), 084102.

[28] T. G. Kolda and B. W. Bader, *Tensor decompositions and applications*, SIAM Rev., 51 (2009), pp. 455–500.

[29] L. R. Tucker, *Some mathematical notes on three-mode factor analysis*, Psychometrika, 3 (1966), pp. 279–311.

[30] L. de Lathauwer, B. de Moor, and J. Vandewalle, *A multilinear singular value decomposition*, SIAM J. Matrix Anal. Appl., 21 (2000), pp. 1253–1278.

[31] S. Le Clainche, J. M. Vega, and J. Soria, *Higher order dynamic mode decomposition of noisy experimental data: The flow structure of a zero-net-mass-flux jet*, Exp. Therm. Fluid Sci., 88 (2017), pp. 336–353.

[32] G. H. Golub and G. T. van Loan, *Matrix Computations*, Johns Hopkins University Press, Baltimore, 1996.

[33] A. Meseguer, *Fundamentals of Numerical Mathematics for Physicists and Engineers*, John Wiley and Sons, New York, 2020.

[34] I. Mercader, O. Batiste, and A. Alonso, *An efficient spectral code for incompressible flows in cylindrical geometries*, Comput. Fluids 39 (2010), pp. 215–224.

[35] S. Hugues and A. Randriamampianina, *An improved projection scheme applied to pseudospectral methods for the incompressible Navier-Stokes equations*, Internat. J. Numer. Methods Fluids, 28 (1998), pp. 501–521.

[36] O. Sánchez, X. Ruiz, M. Pujalte, I. Mercader, O. Batiste, and J. Gavaldà, *On the determination of diffusion coefficients in two-component alloys and doped semiconductors. Several implications concerning the International Space Station*, Int. J. Heat Mass Transfer, 88 (2015), pp. 508–518.

[37] O. Sánchez, I. Mercader, O. Batiste, and A. Alonso, *Natural convection in a horizontal cylinder with axial rotation*, Phys. Rev. E, 93 (2016), 063113.

[38] W. H. Press, S. A. Teukolsky, W. T. Vetterling, and B. P. Flannery, *Numerical Recipes in C: The Art of Scientific Computing*, Cambridge University Press, Cambridge, UK, 1988.

[39] V. I. Arnold, *Geometrical Methods in the Theory of Ordinary Differential Equations*, Springer-Verlag, Berlin, 1983.

[40] I. M. Niven and H. S. Zuckerman, *An Introduction to the Theory of Numbers*, John Wiley and Sons, New York, 1972.